

Bridging Simulation and Experiment: A Self-Supervised Domain Adaptation Framework for Concrete Damage Classification

Chen Xu^a, Giao Vu^a, Ba Trung Cao^{a,1,*}, Zhen Liu^{a,b}, Fabian Diewald^c, Yong Yuan^b, Günther Meschke^a

^a*Institute for Structural Mechanics, Ruhr University Bochum, Universitätsstraße 150, 44801 Bochum, Germany*

^b*Department of Geotechnical Engineering, College of Civil Engineering, Tongji University, 1239 Siping Road, 20092 Shanghai, China*

^c*Centre for Building Materials, Technical University of Munich, 81245 Munich, Germany*

Abstract

Reliable assessment of concrete degradation is critical for ensuring structural safety and longevity of engineering structures. This study proposes a self-supervised domain adaptation framework for robust concrete damage classification using coda wave signals. To support this framework, an advanced virtual testing platform is developed, combining multiscale modeling of concrete degradation with ultrasonic wave propagation simulations. This setup enables the generation of large-scale labeled synthetic data under controlled conditions, reducing the dependency on costly and time-consuming experimental labeling. However, neural networks trained solely on synthetic data often suffer from degraded performance when applied to experimental data due to domain shifts. To bridge this domain gap, the proposed framework integrates domain adversarial training, minimum class confusion loss, and the Bootstrap Your Own Latent (BYOL) strategy. These components work jointly to facilitate effective knowledge transfer from the labeled simulation domain to the unlabeled experimental domain, achieving accurate and reliable damage classification in concrete. Extensive experiments demonstrate that the proposed method achieves notable performance improvements, reaching an accuracy of 0.7762 and a macro F1 score of 0.7713, outperforming both the plain 1D CNN baseline and six representative domain adaptation techniques. Moreover, the method exhibits high robustness across training runs and introduces only minimal additional computational cost. These findings highlight the practical potential of the proposed simulation-driven and label-efficient framework for real-world applications in structural health monitoring.

Keywords: Concrete damage identification, Structural health monitoring, Domain adaptation, Self-supervised learning, Data fusion

^{*}Corresponding author

¹email: ba.cao@rub.de

1. Introduction

In modern civil engineering, concrete structures are fundamental to a wide range of infrastructure projects due to their superior strength, durability, and cost efficiency. Nevertheless, concrete inevitably undergoes degradation over time, threatening the structural reliability and potentially leading to catastrophic failures. Therefore, accurate and efficient structural health monitoring (SHM) of concrete structures remains a critical engineering challenge. Under external loading, degradation of concrete typically initiates with the nucleation of microcracks around aggregates, pores, and inherent defects. As the load increases, these microcracks propagate and coalesce into localized macrocracks, ultimately reducing the load-bearing capacity and resulting in structural failure. Due to their significantly smaller scale compared to aggregates, early-stage microcracks are difficult to detect using conventional SHM techniques.

Ultrasonic-based monitoring techniques are particularly attractive for SHM due to their non-invasive, highly sensitive, and cost-effective nature. Since wave velocity is directly influenced by the elastic properties and microstructure of concrete, ultrasonic measurements can provide insight into the internal state of structural materials. Among these techniques, Coda Wave Interferometry (CWI) (Snieder et al., 2002; Snieder, 2006) has shown great promise. CWI works by comparing wave signals measured before and after perturbations caused by microstructural changes. It has successfully identified subtle damage evolution in a variety of materials under varying external conditions (Planès and Larose, 2013; Wang et al., 2021; Grabke et al., 2021, 2022; Shan et al., 2022; Qu et al., 2023; Liu et al., 2024; Yi et al., 2024; Sträter et al., 2025). With its high sensitivity to slight changes in diffusive media, CWI is able to detect early-stage microcrack initiation and growth, typically beyond the resolution of traditional SHM methods, thus providing a promising approach for early damage detection in concrete structures.

However, the meaningful interpretation of wave features derived from CWI requires in-depth domain knowledge of concrete behavior, as the relationship between signal variations and mechanical state is complex and often non-unique. Such analyses are typically conducted under well-controlled laboratory conditions. Even then, obtaining error-free, labeled datasets that link ultrasonic signals with precise mechanical states remains a challenge. Conversely, numerical simulations offer a more cost-effective and noise-free alternative, but may lack full physical fidelity. These limitations from both experimental and simulation perspectives present a significant challenge for developing robust, generalizable wave-based damage assessment frameworks applicable to real-world scenarios.

Artificial intelligence (AI) technologies are advancing at an incredible pace, reshaping numerous engineering fields. Among recent developments, physics-informed machine learning (PIML) has emerged as a dynamic interdisciplinary field that integrates prior physical knowledge with machine learning algorithms to tackle complex engineering problems (Raissi et al., 2019; Karniadakis et al., 2021; Lu et al., 2021; Xu et al., 2023, 2024).

Inspired by this paradigm, our research aims to leverage simulated data to train classifiers capable of identifying damage states in concrete structures from coda wave signals. To this end, our previous work (Vu et al., 2021b, 2025) employed physics-based numerical

simulations to model the complete damage evolution process in concrete. These simulations generated large volumes of synthetic coda wave data, which were then used to train neural networks for damage state classification. The trained models can be subsequently applied to experimental data collected under real-world conditions.

One of the key advantages of this simulation-driven strategy lies in its ability to considerably reduce the cost and effort associated with collecting labeled experimental data. In many SHM applications, manual labeling is expensive, time-consuming, or even infeasible due to destructive testing requirements and limited access to internal structural states (Liu and Fang, 2024; Wang et al., 2025). By utilizing labeled simulated data, this approach enables concrete damage classification without requiring direct annotation of experimental data, thereby offering a scalable and label-efficient solution for real-world application.

Nevertheless, when neural networks, which have been trained exclusively on simulated data, were tested with real experimental data, a noticeable drop in classification performance was observed. This discrepancy arises primarily from the inevitable simplifications inherent in numerical simulations, which fail to fully replicate the complex cracking behavior of actual concrete structures. As a result, a significant distribution shift (Pan and Yang, 2010; Li et al., 2024) exists between the simulated (source domain) and experimental (target domain) data, which severely limits the model's ability to generalize across domains.

Domain adaptation (DA), as an important subfield of transfer learning, serves as an effective framework for addressing the distribution shift between datasets (Liu et al., 2022). In recent years, several studies have successfully employed DA techniques to transfer knowledge from simulated to experimental domains across various application areas, with machinery fault diagnosis being among the frequently explored topics (Pang et al., 2024; Jiang et al., 2024, 2025; Huang et al., 2025; Zhu et al., 2025; Xiao et al., 2025). Meanwhile, in the field of SHM for civil engineering, Wang et al. (Wang and Xia, 2022) introduced a re-weighted adversarial method to transfer knowledge from finite element models to experimental structures. Giglioni et al. (Giglioni et al., 2024) implement Joint Domain Adaptation and Normal Condition Alignment to align features across real bridges and simulations. Zhang et al. (Zhang et al., 2025) developed a structural damage detection method based on the joint maximum discrepancy and adversarial discriminative domain adaptation (JMDAD), enabling transfer learning between numerical models and physical structures. Talaei et al. (Talaei et al., 2025) combine Maximum Mean Discrepancy and adversarial DA techniques to reduce domain shift and accurately estimate prestress in concrete bridges under moving loads.

Although DA has shown promise, its application to concrete damage classification, particularly with coda wave data, remains at a preliminary stage and requires further investigation (Weng et al., 2023). Moreover, existing studies have not fully exploited the latent representations embedded in the target domain to improve accuracy. In our case, the absence of labeled target domain data during training naturally places the problem within the scope of self-supervised learning (SSL) (Liu et al., 2023; Gui et al., 2024). Among various SSL techniques, contrastive learning has demonstrated strong capabilities in extracting more discriminative feature representations from unlabeled datasets, thereby

enhancing performance in downstream tasks (Gu et al., 2024; Hoxha et al., 2025). Given the lack of labeled experimental data and the need for robust feature representation learning, contrastive learning is well suited to be incorporated as a component of our proposed approach.

In this paper, a domain adaptation framework enhanced with self-supervised learning is proposed to enable reliable knowledge transfer from the simulation domain to the experimental domain. Domain adaptation in our framework is achieved through a combination of Domain-Adversarial Neural Network (DANN) (Ganin et al., 2016; Li et al., 2023) and Minimum Class Confusion (MCC) loss (Jin et al., 2020). DANN promotes domain-invariant feature learning through adversarial training between a domain discriminator and the feature extractor. Meanwhile, the MCC regularization explicitly reduces inter-class confusion within the target domain, promoting more discriminative and well-separated feature representations. In addition, the Bootstrap Your Own Latent (BYOL) method (Grill et al., 2020), an SSL approach, is incorporated to encourage the network to learn meaningful feature representations from unlabeled experimental data. Our approach requires no labeled experimental data and introduces only minimal additional computational overhead, yet substantially improves the performance of concrete damage classification when applied to real-world experimental scenarios.

The structure of this paper is as follows: Section 2 summarizes the computational simulations used to generate synthetic data and Section 3 details the proposed domain adaptation framework with self-supervised learning. Section 4 introduces the generation of both simulated data and experimental data for concrete damage classification, and Section 5 demonstrates the performance of the proposed method in predicting concrete damage in real-world scenarios. Finally, Section 6 summarizes the main findings, discusses the limitations, and suggests directions for future research.

2. A Simulation-based Platform for Damage Assessment in Concrete

To generate synthetic data for training, a simulation-based virtual testing platform developed in (Vu et al., 2025) is employed. The process begins with the creation of a realistic concrete specimen using an in-house Concrete Mesostructure Generator. The mechanical response of the specimen under uniaxial compression is simulated using a multiscale reduced-order model. At the microscale, microcrack initiation and propagation are modeled within the framework of Linear Elastic Fracture Mechanics (LEFM). At the mesoscale, the corresponding stress and strain fields are computed by solving the integral form of the Lippmann–Schwinger equations, as detailed in (Vu et al., 2021a, 2025). These deformation snapshots are then used as input for finite difference simulations of ultrasonic wave propagation under multiple source-receiver configurations (Saenger et al., 2005; Schepp et al., 2020). A CWI-based analysis is performed to evaluate wavefield changes in response to mechanical loading, enabling comparison with experimental trends and providing labeled damage states for supervised learning. Finally, spatially informative patterns are captured from the simulated ultrasonic signals using two-point statistical correlations, forming the input for classification. The overall computational workflow is illustrated in Figure 1.

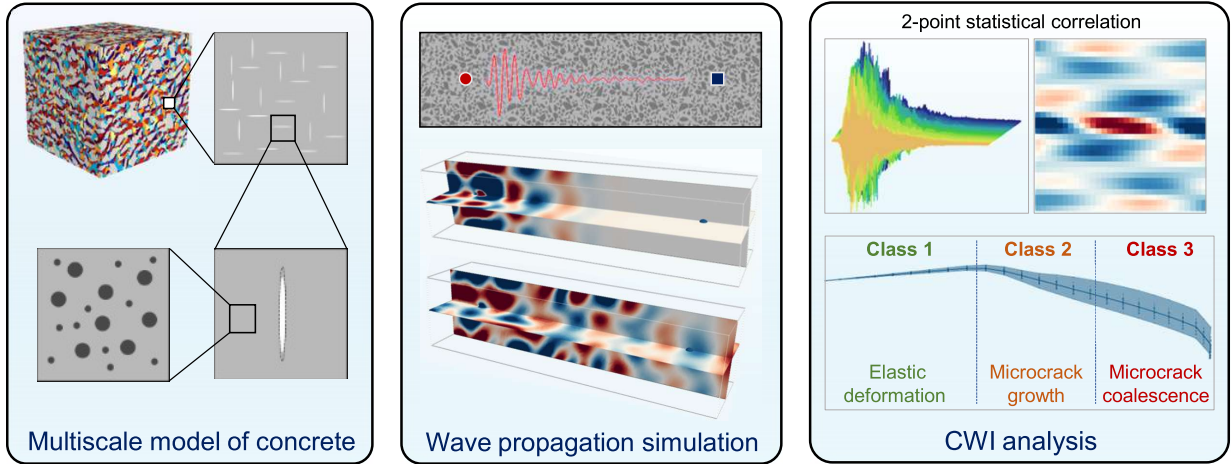


Figure 1: Workflow of the virtual testing platform for damage assessment in concrete structures.

2.1. Multiscale and Ultrasonic Wave Propagation Simulation in Concrete

Multiscale modeling. Multiscale modeling offers a rigorous, physics-based approach to linking the macroscopic material behavior in concrete with its underlying microstructural evolution during loading, without the need for empirical assumptions (Matouš et al., 2017). It operates through two fundamental mechanisms: homogenization, which transfers microscale mechanical properties (e.g., stiffness and stress) to the macroscale, and localization, which maps macroscopic strain fields back to the microstructure. This bidirectional coupling enables accurate simulation of complex damage phenomena across scales.

Homogenization, which is typically computationally intensive in multiscale modeling, is addressed using a k-means clustering-based model reduction technique. This method groups similar material points and assigns each cluster a representative subproblem, thereby improving computational efficiency (Liu et al., 2016). The concrete mesostructure is discretized using a voxel-based representation, in which aggregates and mortar are explicitly resolved. At the microscale, the mortar matrix contains three orthogonal families of penny-shaped microcracks, each characterized by specific orientation, volume fraction, radius, and thickness. These microcracks serve as the principal mechanism for simulating diffuse damage under compressive loading.

Localization is performed by solving the Lippmann–Schwinger equation to compute mesoscopic strain fields, which in turn drive microcrack evolution based on Linear Elastic Fracture Mechanics. Homogenization then updates the macroscopic stiffness tensor using a modified Interaction Direct Derivative with evolving microcrack distribution (Vu et al., 2021a). Despite using a simplified crack representation, the model effectively captures load-induced anisotropy and early-stage damage in concrete.

Wave propagation modeling. Wave propagation is modeled by solving elastodynamic wave equations using finite difference schemes on Rotated Staggered Grids (Schepp et al., 2020). To account for the decaying characteristics of ultrasonic wave fields traversing through concrete, a viscoelastic material model with two Maxwell bodies is employed (Saenger

et al., 2005). The ultrasonic wave source is modeled as a six-component tensor to accurately replicate the radiation pattern of real transducers. Meanwhile, the recorded signals are the temporal stresses over a prescribed time interval.

2.2. Coda Wave Interferometry (CWI) for Generating Training Outputs

Relative velocity variation (dv/v) and cross-correlation (CC) are key metrics for quantifying time shifts and waveform similarity in ultrasonic and seismic signals. The dv/v metric captures subtle, uniform changes in wave speed linked to microstructural changes, such as crack closure, compaction, or microcracking, while a decrease in the CC signal is well suited to indicate heterogeneous changes of the microstructure, such as localized cracking or stress-induced anisotropy. In this study, dv/v is computed using the stretching technique, which aligns perturbed and reference signals by adjusting a stretch factor α (Niederleithinger et al., 2018). The value of α that maximizes the CC between the two signals is taken as the dv/v . The dv/v metric serves as a reliable indicator for detecting and classifying internal damage in concrete and is calculated as:

$$\frac{dv}{v} = \arg \max_{\alpha \in \mathbb{R}} \text{CC}(\alpha) = \arg \max_{\alpha \in \mathbb{R}} \frac{\int_{t_1}^{t_2} u_u(t) u_p(t(1 + \alpha)) dt}{\sqrt{\int_{t_1}^{t_2} u_u^2(t) dt \int_{t_1}^{t_2} u_p^2(t(1 + \alpha)) dt}} \times 100\%. \quad (1)$$

As a preliminary analysis, CWI is employed to study the influence of material degradation on ultrasonic wave velocity variations. By comparing numerical and experimental results, it serves as a practical tool to validate the mechanical–ultrasonic coupling implemented in the simulations. However, while the obtained relative velocity changes provide good indication regarding the intensity of material degradation, the state of degradation cannot be directly derived.

2.3. Two-Point Statistical Correlation for Generating Training Inputs

Traditional CWI features, such as dv/v and CC, effectively capture global variations in signals but provide limited insight into specific damage mechanisms. Two-point statistics, however, yield richer and more detailed information on the type and severity of damage by capturing spatial correlations within the ultrasonic waveforms (Cecen et al., 2016; Brough et al., 2017). Their high dimensionality also enhances sensitivity and robustness to noise, making them effective for machine learning-based damage classification tasks. To compute two-point statistics from 1D ultrasonic signals, consider two normalized ultrasonic waveforms: a reference signal $\tilde{u}_u[t]$ and a perturbed signal $\tilde{u}_p[t]$. The two-point correlation function is obtained by correlating these signals across discrete temporal shifts. Specifically, the statistics is calculated as follows:

$$f[\chi] = \frac{1}{\delta[\chi]} \sum_t \tilde{u}_u[t] \tilde{u}_p[t + \chi], \quad (2)$$

where χ denotes the discrete time lag in the one-dimensional temporal domain, and the normalization factor $\delta[\tau]$ accounts for variations in the number of overlapping samples at

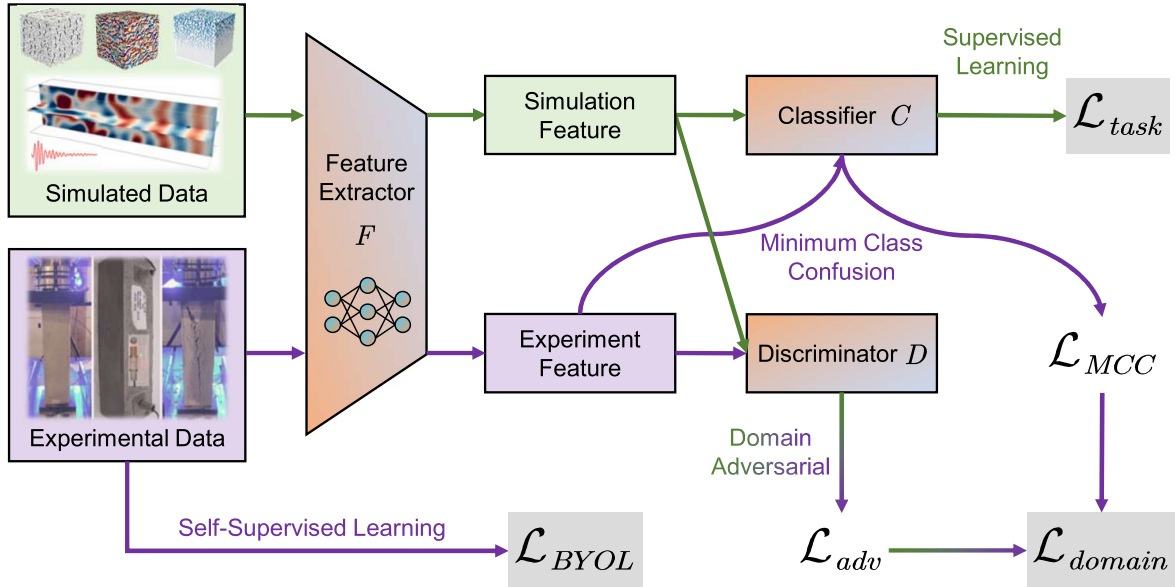


Figure 2: Schematic of the proposed self-supervised domain adaptation framework for concrete damage classification using coda wave signals. The architecture integrates supervised learning on simulated data with domain adversarial training, minimum class confusion (MCC), and self-supervised BYOL strategy on experimental data. These components work synergistically to align feature distributions and improve generalization across domains.

each lag. By directly utilizing this correlation approach, the resulting two-point statistics effectively encode detailed temporal features, facilitating accurate detection and classification of subtle structural changes.

3. The Proposed Self-Supervised Domain Adaptation Framework

The fundamental concepts behind our proposed framework are presented in detail in the following subsections. A schematic of the entire framework is illustrated in Fig. 2, highlighting each major component and the data flow between them. The proposed framework consists of a shared feature extractor F , a classifier C , and a domain discriminator D , jointly trained using both simulated and experimental data. The classifier C learns under supervision from the labeled simulation data, while the discriminator D encourages domain-invariant feature learning through adversarial training and the MCC objective. In parallel, a BYOL branch introduces self-supervised learning on the experimental data to improve feature representations without requiring labels. All modules are concurrently optimized through three loss components: \mathcal{L}_{task} , \mathcal{L}_{domain} , and \mathcal{L}_{BYOL} , enabling robust knowledge transfer from simulation to experiment.

3.1. 1D Convolutional Neural Network (CNN) for Classification

Let us first focus on the most fundamental component for the classification task: a 1D CNN. With its extraordinary performance, the 1D CNN has become the *de facto* standard

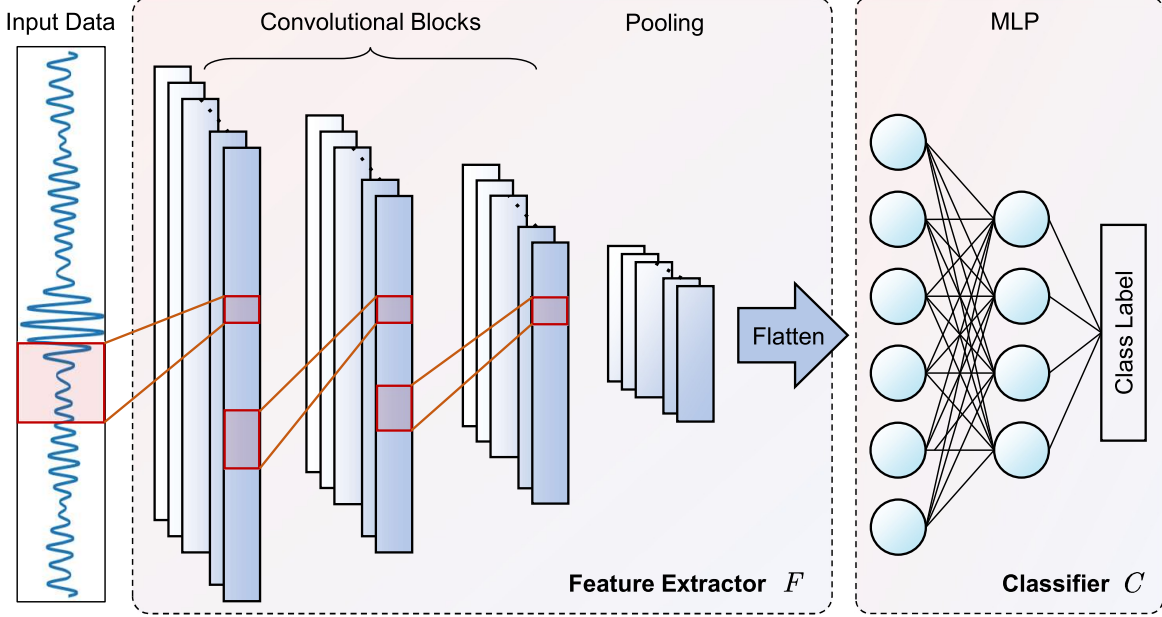


Figure 3: Architecture of a 1D CNN model consisting of a convolutional feature extractor F and an MLP classifier C .

architecture for signal processing across various research areas (Kiranyaz et al., 2021; Li et al., 2022; Xiong et al., 2025).

As illustrated in Fig. 3, a 1D CNN can be viewed as a combination of a feature extractor F and a classifier C . The feature extractor F is designed to extract feature representations from the input data and comprises several stacked convolutional blocks. In each block (shown in Fig. 4), the 1D convolutional layers (Conv1d) can extract local features by sliding convolutional kernels over the input and capture spatial information through parameter sharing. Each convolutional layer is followed by a batch normalization layer and a rectified linear unit (ReLU) activation function. Subsequently, a pooling layer is employed to reduce the dimensionality of the data, and the output is then flattened to obtain the extracted features. The classifier C , implemented as a multi-layer perceptron (MLP), finally processes the features from F and assigns them to appropriate classes.

The dataset obtained from numerical simulation is denoted as $\mathcal{D}_s = \{x_i^s, y_i^s\}_{i=1}^{N_s}$, with its underlying data distribution represented by p_s , where the subscript s stands for source domain. A 1D CNN is trained on \mathcal{D}_s in a fully supervised manner. The input samples x^s are first processed by the feature extractor F , and the resulting features are fed into the classifier C to produce the predicted labels $C(F(x^s))$. The model is optimized by minimizing the cross-entropy loss ℓ between the predicted labels and the corresponding ground-truth labels y^s . The supervised classification loss is therefore formulated as follows:

$$\mathcal{L}_{task}(F, C) = \mathbb{E}_{(x,y) \sim p_s} [\ell(C(F(x)), y)]. \quad (3)$$

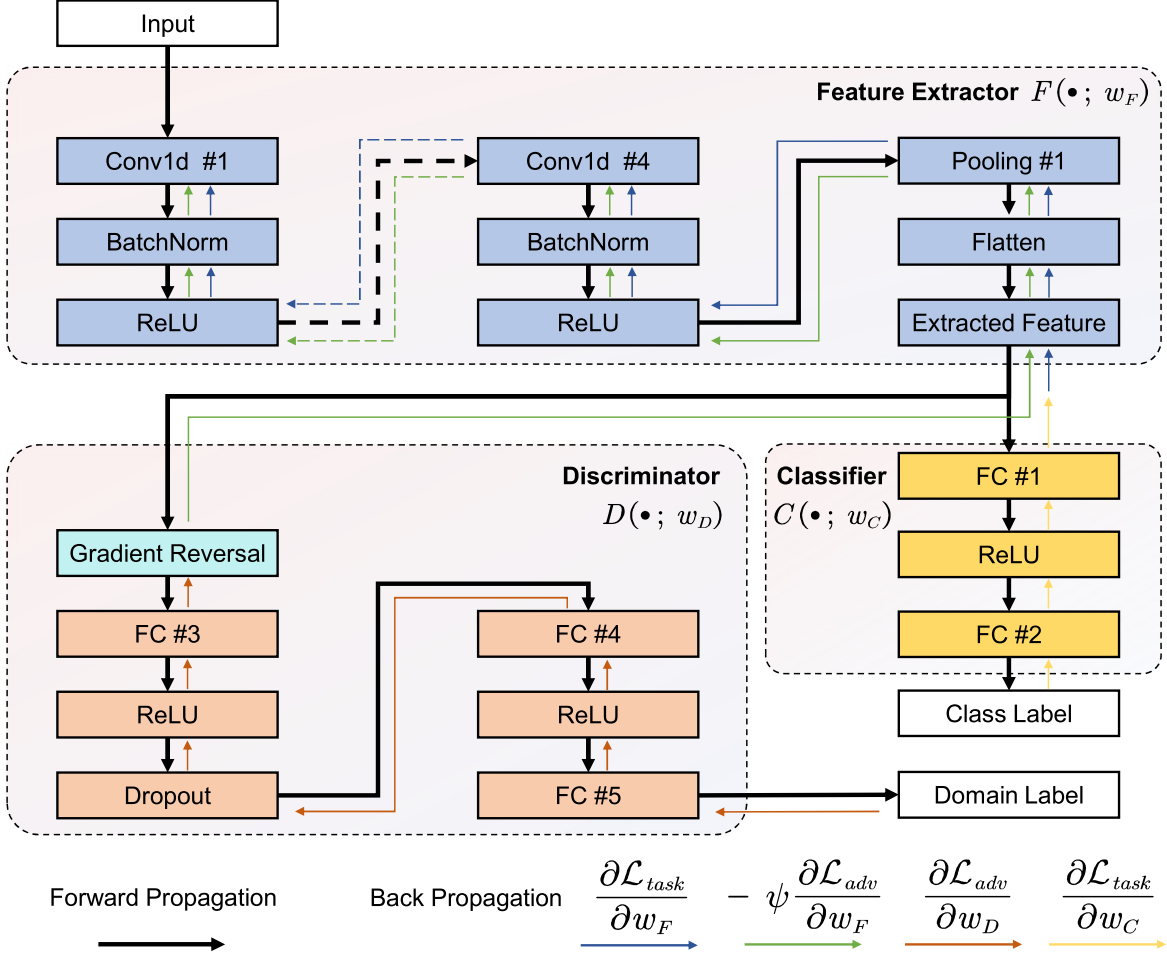


Figure 4: Detailed architecture of the domain adversarial training module within the proposed framework, including a feature extractor $F(\cdot; w_F)$, a classifier $C(\cdot; w_C)$, and a domain discriminator $D(\cdot; w_D)$. Forward propagation paths are shown in black, while colored arrows indicate component-specific gradient flows during backpropagation. Detailed layer-wise configurations for convolutional (Conv1d) and fully connected (FC) layers are provided in Table 1.

3.2. Adversarial Domain Adaptation with Minimum Class Confusion (MCC)

The dataset obtained from experiment is denoted as $\mathcal{D}_t = \{x_i^t, y_i^t\}_{i=1}^{N_t}$, with its corresponding data distribution being p_t , where the subscript t stands for target domain. When there is a discrepancy between the data distributions of the source and target domains ($p_s \neq p_t$), also referred to as domain shift (Pan and Yang, 2010), directly applying the model trained on the source domain (i.e. the simulation-based 1D CNN described in Section 3.1) leads to a significant performance degradation on the target domain (experimental data). To tackle this problem, the DANN proposed in (Ganin et al., 2016) is adopted to achieve domain adaptation. This approach forces the model to learn features that are robust to domain shifts, thereby enhancing its generalization capability on the target domain. As shown in Fig. 4, a third component is introduced, namely the domain discriminator D , which establishes an adversarial training process between the feature extractor F and

the discriminator D . The discriminator takes the extracted features as input and outputs domain labels, where the labels for the source and target domains are set to 0 and 1, respectively. The loss function of DANNs can be written as:

$$\mathcal{L}_{adv}(F, D) = \mathbb{E}_{x \sim p_s} [\ell(D(F(x)), 0)] + \mathbb{E}_{x \sim p_t} [\ell(D(F(x)), 1)]. \quad (4)$$

The underlying idea behind Eq. (4) is that the domain discriminator D continuously improves its ability to distinguish between features from the source and target domains by minimizing \mathcal{L}_{adv} , while the feature extractor F aims to learn features that are hard for the discriminator D to differentiate by maximizing \mathcal{L}_{adv} . This adversarial setup gives rise to a minimax game between two players F and D , which compels the model to extract domain-invariant features that perform well across both the source and target domains. To achieve this, as shown in Fig. 4, a Gradient Reversal Layer (GRL) is inserted at the beginning of the domain discriminator D . The GRL serves as an identity function during forward propagation, but during backpropagation it multiplies the gradient by a negative constant $-\psi$ (where $\psi > 0$ is a hyperparameter controlling the adversarial strength), that is:

$$R_\psi(k) = k, \quad \frac{\partial R_\psi(k)}{\partial k} = -\psi I. \quad (5)$$

In order to alleviate class ambiguity in the target domain, the Minimum Class Confusion (MCC) loss (Jin et al., 2020) is introduced as a complementary component to the domain adaptation process. Unlike conventional feature alignment strategies that operate in the latent feature space, MCC directly works on the output logits of classifier. It strives to reduce pairwise confusion among classes by leveraging the output distribution, thus encouraging clearer decision boundaries in the target domain. The whole procedure for computing the MCC loss is illustrated in Fig. 5.

Let $\mathbf{A} \in \mathbb{R}^{N_b \times |\mathcal{C}|}$ denote the classifier logits for a batch of N_b unlabeled target domain samples, where $|\mathcal{C}|$ is the number of classes. To prevent overconfident predictions from dominating the confusion estimation, a temperature scaling technique is applied to calibrate the logits:

$$\hat{B}_{ij} = \frac{\exp(A_{ij}/T)}{\sum_{j'=1}^{|\mathcal{C}|} \exp(A_{ij'}/T)}, \quad (6)$$

where T is a temperature hyperparameter controlling the smoothness of the prediction probabilities, and \hat{B}_{ij} represents the probability that the i -th sample in the batch belongs to class j .

Following the probability rescaling step, MCC constructs a preliminary class correlation matrix to quantify the degree to which two classes are simultaneously activated in the model's predictions:

$$\Omega_{jj'} = \hat{\mathbf{b}}_{.j}^\top \hat{\mathbf{b}}_{.j'}, \quad (7)$$

where $\hat{\mathbf{b}}_{.j} \in \mathbb{R}^{N_b}$ contains the predicted probabilities for class j across the batch. A higher value of $\Omega_{jj'}$ indicates that the model tends to assign high probabilities to both class j and class j' for the same set of samples, which reflects greater ambiguity between these two classes.

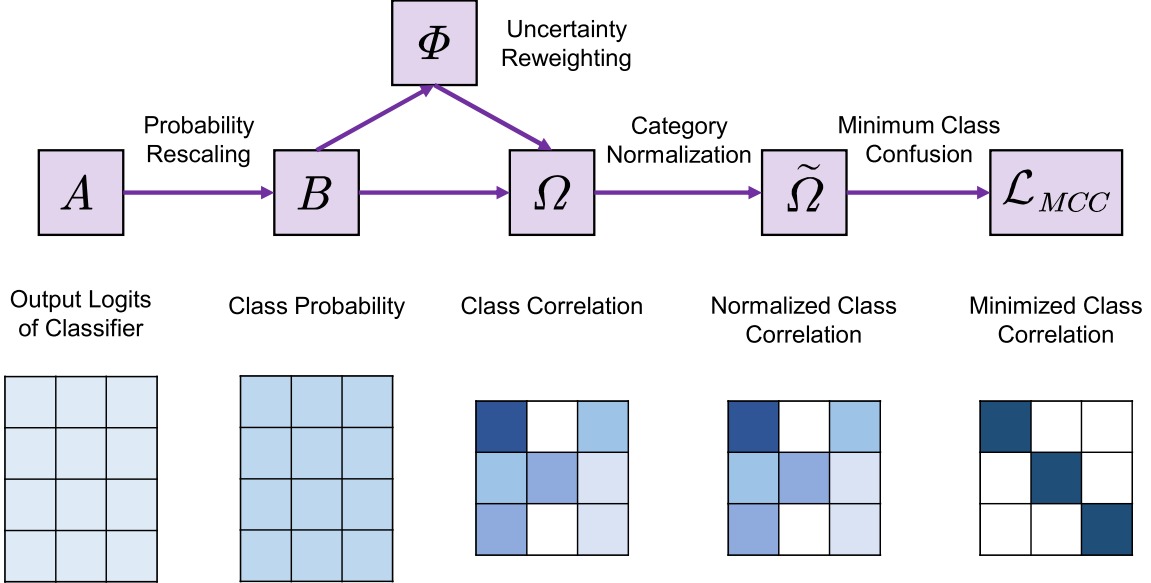


Figure 5: Overview of the Minimum Class Confusion (MCC) loss computation.

Since not all samples contribute equally to the estimation of class confusion, MCC employs an entropy-based weighting mechanism. The entropy (uncertainty) of the prediction $\hat{\mathbf{b}}_i \in \mathbb{R}^{|\mathcal{C}|}$ of sample i is computed as

$$H(\hat{\mathbf{b}}_{i \cdot}) = - \sum_{j=1}^{|\mathcal{C}|} \hat{B}_{ij} \log \hat{B}_{ij}, \quad (8)$$

based on this entropy, a weight reflecting the importance of sample i in modeling class confusion is defined as

$$\Phi_{ii} = \frac{N_b \left(1 + \exp \left(-H(\hat{\mathbf{b}}_{i \cdot}) \right) \right)}{\sum_{i'=1}^{N_b} \left(1 + \exp \left(-H(\hat{\mathbf{b}}_{i \cdot}) \right) \right)}, \quad (9)$$

with this uncertainty reweighting, the refined class correlation is given by:

$$\Omega_{jj'} = \hat{\mathbf{b}}_{\cdot j}^\top \Phi \hat{\mathbf{b}}_{\cdot j'}, \quad (10)$$

where Φ is the corresponding diagonal matrix for Φ_{ii} .

To mitigate class imbalance within each batch, the refined correlation undergoes an additional step of category normalization:

$$\tilde{\Omega}_{jj'} = \frac{\Omega_{jj'}}{\sum_{j''=1}^{|\mathcal{C}|} \Omega_{jj''}}, \quad (11)$$

the resulting $\tilde{\Omega}_{jj'}$ can effectively capture the confusion between class j and j' . The MCC loss is then computed as the average normalized confusion between all pairs of different

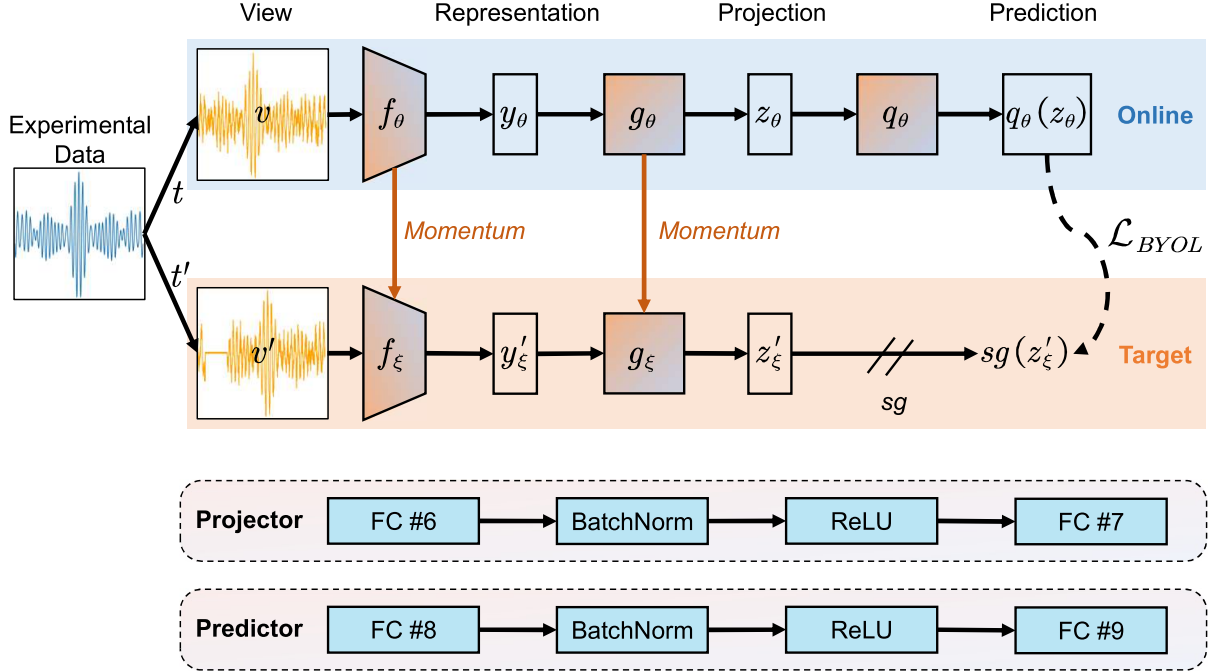


Figure 6: Architecture of the BYOL-based self-supervised learning module. The layer configurations of fully connected (FC) layers in the projector and predictor are detailed in Table 1.

classes:

$$\mathcal{L}_{MCC} = \frac{1}{|\mathcal{C}|} \sum_{j=1}^{|\mathcal{C}|} \sum_{j' \neq j} \tilde{\Omega}_{jj'}. \quad (12)$$

The final domain adaptation objective combines both the adversarial loss in Eq. (4) and the MCC loss in Eq. (12), and is expressed as:

$$\mathcal{L}_{domain} = \mathcal{L}_{adv} + \mathcal{L}_{MCC}, \quad (13)$$

3.3. Self-Supervised Learning: Bootstrap Your Own Latent (BYOL)

In order to further extract experimental features that are more meaningful for the downstream classification task, a SSL method known as BYOL (Grill et al., 2020) is adopted. Its core idea is to learn useful feature representations by aligning two sets of networks, rather than relying on contrasting negative pairs (He et al., 2020; Chen et al., 2020).

BYOL consists of an online network and a target network, with their detailed architecture depicted in Fig. 6. The online network is composed of an encoder f_θ , a projection head g_θ , and a predictor q_θ ; while the target network only contains an encoder f_ξ and a projection head g_ξ . The encoders of both the online and target networks adopt the identical architecture as the feature extractor F described in Sections 3.1 and 3.2. Notably, the encoder f_θ of the online network shares its network parameters with the feature extractor F . The projection heads and predictor are implemented as MLPs.

For each input sample, two different views v and v' are generated through random data augmentations t and t' , respectively. The view v is input into the online network

where it is first transformed into a primary feature representation h_θ by the encoder f_θ , then mapped to z_θ via the projection head g_θ , and finally processed by the predictor q_θ to produce the prediction $q_\theta(z_\theta)$. The computation process for v' in the target network follows a similar procedure to that of the online network, except that the predictor is excluded. The objective of BYOL is to make the online network's prediction $q_\theta(z_\theta)$ to approximate the target network's projection z'_ξ . To this end, mean squared error is used as the loss function, which can be expressed as:

$$\mathcal{L}_{BYOL} = \left\| \frac{q_\theta(z_\theta)}{\|q_\theta(z_\theta)\|_2} - \frac{z'_\xi}{\|z'_\xi\|_2} \right\|_2^2 = 2 - 2 \cdot \frac{\langle q_\theta(z_\theta), z'_\xi \rangle}{\|q_\theta(z_\theta)\|_2 \|z'_\xi\|_2}. \quad (14)$$

The parameters θ of the online network are updated by optimizing the training loss through gradient descent, while the target network parameters ξ are not directly updated. Instead, they are updated using an Exponential Moving Average (EMA) method as follows:

$$\xi \leftarrow \tau \xi + (1 - \tau) \theta, \quad (15)$$

where τ is the momentum coefficient.

3.4. Model Training and Evaluation

The proposed method encompasses a total of seven neural network components: the encoder of the online network f_θ (which is equivalent to the feature extractor F), the projection head of the online network g_θ , the predictor of the online network q_θ , the encoder of the target network f_ξ , the projection head of the target network g_ξ , the classifier C , and the domain discriminator D . Table 1 provides detailed parameter settings for all of these components. The overall loss function is given by

$$\mathcal{L}_{total} = \mathcal{L}_{task} + \mathcal{L}_{domain} + \mathcal{L}_{BYOL}. \quad (16)$$

The parameters were optimized using the Adam optimizer, and all hyperparameter details are provided in Table 2. All the input data have to be scaled in the range of (-1, 1) by min-max normalization. The data augmentation employed in BYOL consists of Gaussian noise addition and random shifting. Specifically, Gaussian noise with a magnitude of 0.1 is added to the signal. Each signal is circularly shifted by a random integer value within $\pm 10\%$ of its total length. All machine learning processes were implemented in Pytorch and trained on an NVIDIA T4 GPU via Google Colab.

The performance of the proposed model is evaluated using two metrics: accuracy and the macro F1 score, with their calculation formulas given below:

$$Accuracy = \frac{TP_1 + TP_2 + TP_3}{N_s + N_t}, \quad (17)$$

$$Precision_i = \frac{TP_i}{TP_i + FP_i}, \quad Recall_i = \frac{TP_i}{TP_i + FN_i}, \quad (18)$$

$$F1_i = 2 \times \frac{Precision_i \times Recall_i}{Precision_i + Recall_i}, \quad (19)$$

Table 1: Layer-wise configuration of neural networks used in the proposed method.

Name of Layer	Setting
Conv1d #1	nn.Conv1d(1, 16, kernel_size=9, stride=2, padding=4)
Conv1d #2	nn.Conv1d(16, 32, kernel_size=7, stride=2, padding=3)
Conv1d #3	nn.Conv1d(32, 32, kernel_size=5, stride=2, padding=2)
Conv1d #4	nn.Conv1d(32, 32, kernel_size=3, stride=2, padding=1)
Pooling #1	nn.AdaptiveAvgPool1d(16)
FC #1	nn.Linear(512, 32)
FC #2	nn.Linear(32, 3)
FC #3 and FC #6	nn.Linear(512, 256)
FC #4	nn.Linear(256, 64)
FC #5	nn.Linear(64, 1)
FC #7 and FC #9	nn.Linear(256, 128)
FC #8	nn.Linear(128, 256)

Table 2: Hyperparameters settings in the codes.

Parameter	Value
Training epochs	500
Batch size	128
Learning rate (except D)	5.00e-05
Learning rate (for D)	1.00e-05
Weight decay	1.00e-04
ψ	1.0
T	2.5
τ	0.99

$$Macro\ F1 = (F1_1 + F1_2 + F1_3) / 3, \quad (20)$$

here, the index i indicates the class, TP_i (True Positives) denotes the number of positive samples that are correctly predicted, TN_i (True Negatives) represents the number of negative samples that are correctly predicted, FP_i (False Positives) is the number of negative samples that are incorrectly predicted as positive, and FN_i (False Negatives) is the number of positive samples that are incorrectly predicted as negative.

4. Data Preparation

4.1. Laboratory Tests for Experimental Dataset (Target Domain)

The experiment data used in this paper is taken from (Diewald et al., 2022). All experiments were performed using a consistent concrete mix composed of ordinary Portland cement (350 kg/m³, water–cement ratio 0.45) and quartzitic crushed aggregates graded according to an AB8 curve. A polycarboxylatether-based superplasticizer was added to

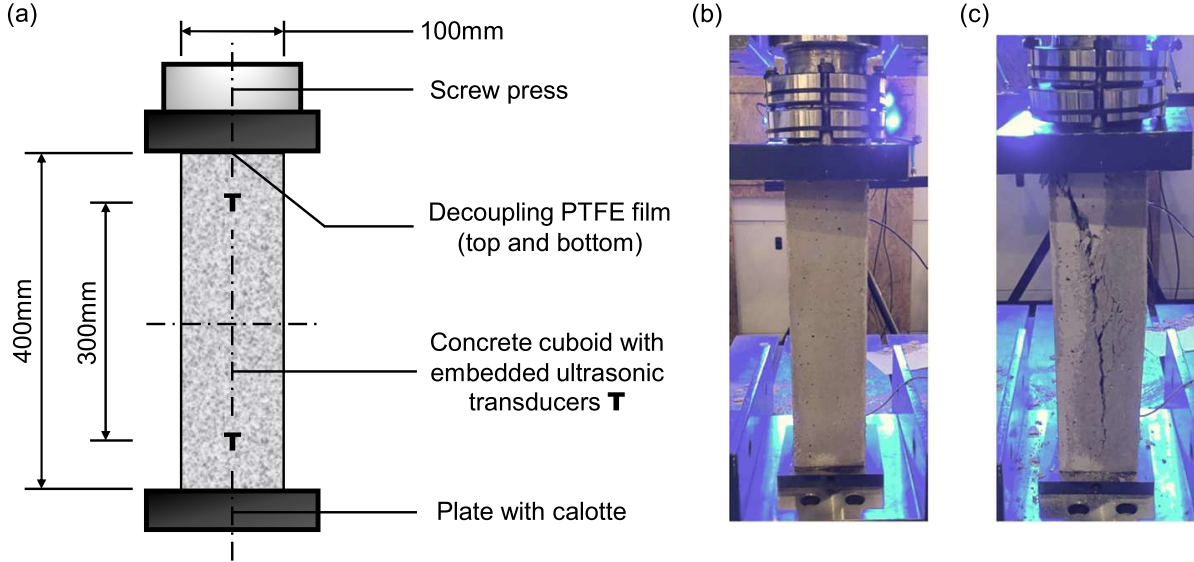


Figure 7: Experimental setup for the uniaxial compression test: (a) schematic of the concrete specimen with dimensions, (b) photo of a specimen during loading, and (c) photo of a specimen after failure.

improve workability and reduce paste viscosity, ensuring proper coupling between embedded sensors and the matrix. The Young's modulus obtained from pre-tests was 84.6 GPa for the quartzitic aggregates and 27.1 GPa for the mortar, while the Poisson's ratio was 0.12 and 0.19, respectively. Compressive strengths were measured as 368.0 MPa for the aggregates and 80.3 MPa for the mortar. The fresh concrete had an air void content of 3.9%. Specimens were water-cured at 20 °C for 7 days, followed by storage at 65% RH and 20 °C. All experiments were carried out 28 days after casting.

As shown in Fig. 7, three cuboid specimens (100 × 100 × 400 mm) were used for the compression tests, each equipped with a pair of transducers symmetrically positioned 300 mm apart. To minimize friction and prevent multiaxial stress near the end faces, PTFE films were placed between the sawn specimen ends and the hydraulic press. The average compressive strength of three identical reference specimens without embedded transducers was measured to be $f_c = 42.9$ MPa. Each test began with a 5% f_c preload to relieve internal stresses, followed by uniaxial compressive loading at 50 N/s. Ultrasonic signals were collected at a rate of 0.1 Hz. Maximum loads of 100%, 60%, and 30% of the compressive strength f_c were applied to the three specimens, respectively, after which each was unloaded at 50 N/s.

The relative velocity change (dv/v) was evaluated using a fixed, non-perturbed reference signal obtained at the unloaded state. Both parameters were analyzed as a function of compressive stress during the uniaxial loading process for three specimens subjected to different maximum loads, as shown in Fig. 8. The results show that the dv/v increases with increasing load up to 60% of f_c (25.6 MPa), after which a decline is observed, indicating the beginning of material damage. For the two non-failed specimens, unloading led to a partial recovery of dv/v , reaching 0.6% and 0.9% for the 30% and 60% f_c cases, respec-

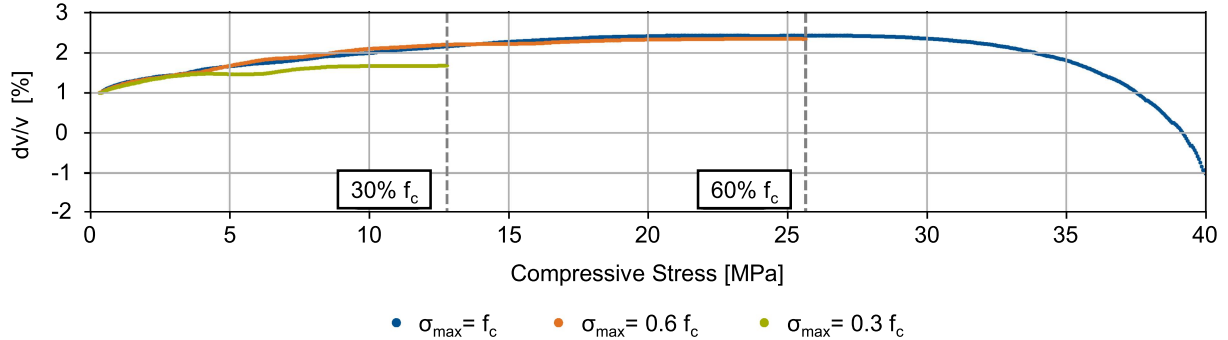


Figure 8: Relative velocity change (dv/v) and signal correlation coefficient (CC) for three specimens in laboratory tests, presented with respect to compressive stress during loading up to 100%, 60%, and 30% of the compressive strength f_c .

tively, indicating irreversible microstructural changes. Finally, a total of 2133 samples were collected in the experimental dataset \mathcal{D}_t , with 753 for Class 1, 979 for Class 2, and 401 for Class 3.

4.2. Numerical Modeling for Simulated Dataset (Source Domain)

4.2.1. Multiscale Simulation Model

The synthetic data in this paper is generated from the simulation examples presented in (Vu et al., 2025). The examples show synthetic samples replicating experimental concrete specimens from Section 4.1, see Figure 9(a). High-resolution voxel-based models were constructed using 201^3 voxels at a resolution of 0.5 mm. Aggregates larger than 3 mm were explicitly resolved, achieving a 35% volume fraction with a standard deviation of 2.26%, closely matching the experimentally measured particle size distribution. Smaller aggregates (volume fraction 35.5%) were embedded within the hardened cement paste matrix using the Mori-Tanaka homogenization scheme to form the mortar phase. It can be seen in Figure 9(b) that comparison with experimentally measured distribution shows good agreement. The multiscale model of concrete under compression is summarized as follows. The model assumes that both mortar and aggregate contain three mutually orthogonal microcrack families, each defined by specific orientations, topology, and densities. During the initial stage of compressive loading, microcracks oriented perpendicular to the loading direction tend to close partially, resulting in a slight increase in stiffness. As the load increases to medium and high levels, lateral expansion induces tensile stresses in the transverse directions. This promotes the propagation of microcracks, whose evolution follows the principles of Linear Elastic Fracture Mechanics (LEFM). At the macroscopic scale, this process manifests as progressive stiffness degradation. Further details can be referred to in Vu et al. (2021a, 2025).

To manage computational complexity, the voxel data were reduced to 72 representative clusters, with 64 for mortar and 8 for aggregates, reducing the model from over 8 million material points to a tractable size without compromising accuracy. Figure 9(c) illustrates the validation of the multiscale simulation model in a prior study (Vu et al., 2021a) for

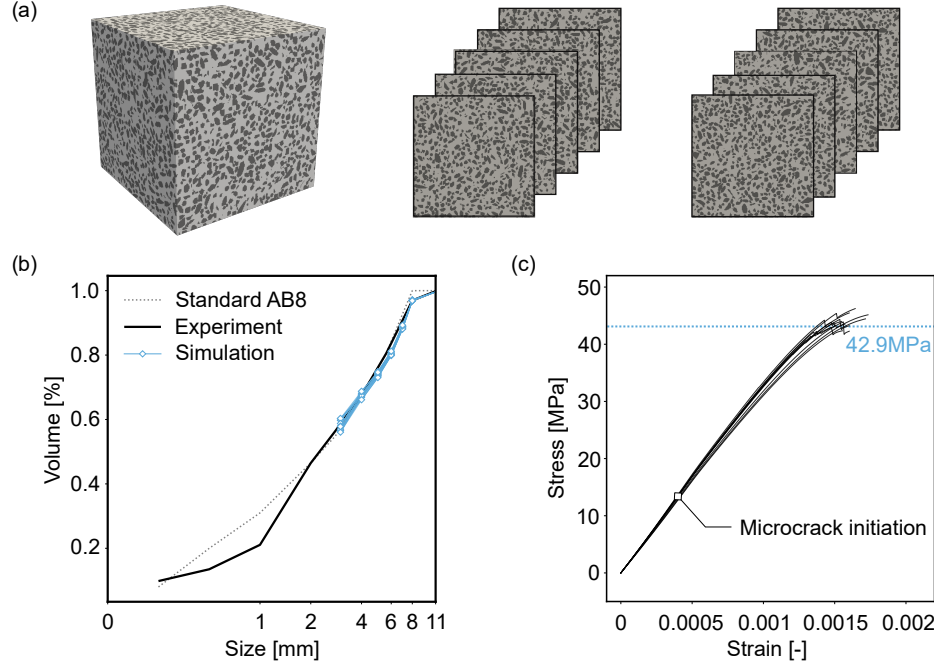


Figure 9: Multiscale model for concrete specimen. (a) A virtual concrete specimen with representative 2D slices; (b) Validation for volume distribution of aggregates; (c) Validation for stress-strain response of concrete specimen under uniaxial compression.

stress-strain response of concrete specimen under uniaxial compression, offers a robust balance between computational efficiency and fidelity. In total, 10 concrete specimens of size 10 cm with a maximum grain size 8 mm (standard AB8) are generated for the test considering the varying of aggregate inside the concrete specimen.

4.2.2. Ultrasonic Wave Propagation Simulation

The multiscale model from Section 4.2.1 is used to simulate the propagation of ultrasonic wave fields through virtual specimens. The simulation is designed around prismatic concrete specimens measuring $10 \times 10 \times 40$ cm, subjected to uniaxial compression with strain increments of 6×10^{-5} , see Figure 10(a). The specimen dimensions ensure that the ultrasonic transducers are placed at least three wavelengths away from the source, minimizing near-field effects and boundary interference. The specimen's high height-to-width ratio reduces frictional influences, allowing the mechanical behavior to closely represent that of real concrete. The ultrasonic excitation uses a moment tensor source with two non-zero components (in a 2D model configuration) and a central frequency of 65 kHz, which approximates the actual transducer emission. Data acquisition employs 27 receivers arranged across three parallel planes located 27.5, 30.0, and 32.5 cm from the source, with a spacing of 2.5 cm between receivers on each plane, as depicted in Figure 10(a). Ultrasonic wave propagation in three dimensions is simulated using a rotated staggered-grid finite-difference method. The simulation runs for 40,000 time steps, covering a total duration of 2 milliseconds. A spatial grid resolution of 0.5 mm and a temporal step size of

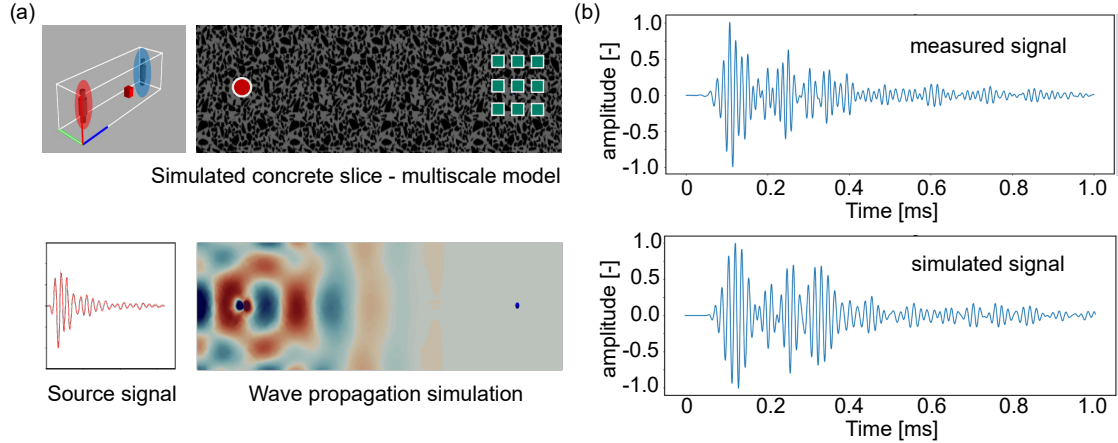


Figure 10: Wave propagation simulation in concrete. (a) Summary of the 3D simulation setup; (b) Validation of simulated wave signals.

5×10^{-8} seconds are employed. To account for the attenuation effects commonly observed in ultrasonic experiments, a viscoelastic model is incorporated, which involves four additional parameters as detailed in (Saenger et al., 2005). To emulate reflective boundary conditions, two vacuum layers are added around all surfaces of the concrete model. As demonstrated in Figure 10(b), the simulated signal exhibit strong qualitative agreement with experimental data, especially in terms of the amplitude decay over time.

4.2.3. CWI Analysis

Prior to dataset generation for the classification task, two essential preparatory steps are undertaken. First, ultrasonic wave propagation simulations in concrete are validated by comparing CWI-derived metrics from simulations with experimental results. This ensures that the simulated signals accurately capture the waveform changes associated with damage progression. This step ensures that the simulated signals reliably capture the evolution of waveforms associated with damage progression, as observed in the experimental data. The second entails the interpretation of CWI-derived metrics to classify potential damage states in concrete subjected to uniaxial compressive loading.

For the validation step, the relative velocity change (dv/v) at a specific time window from 0.2 ms to 0.5 ms is plotted as a function of applied stress, as illustrated in Figure 11(a). Both simulation and experimental data indicate a peak in dv/v occurring at approximately 35% of the peak stress. However, the numerical model does not fully capture the gradual decline in dv/v observed during the micro-cracking regime, nor the pronounced reduction evident beyond 80% of the concrete strength. These discrepancies may be attributed to several model limitations, including the absence of stable crack propagation mechanisms at interfacial transition zones, an idealized representation of microcrack distributions, and simplified assumptions regarding wave source characteristics and signal recording. Despite these simplifications, the numerical results exhibit a generally acceptable level of agreement with experimental observations, particularly in terms of capturing the qualitative trend of velocity evolution with increasing stress. This level of correspondence supports the use of

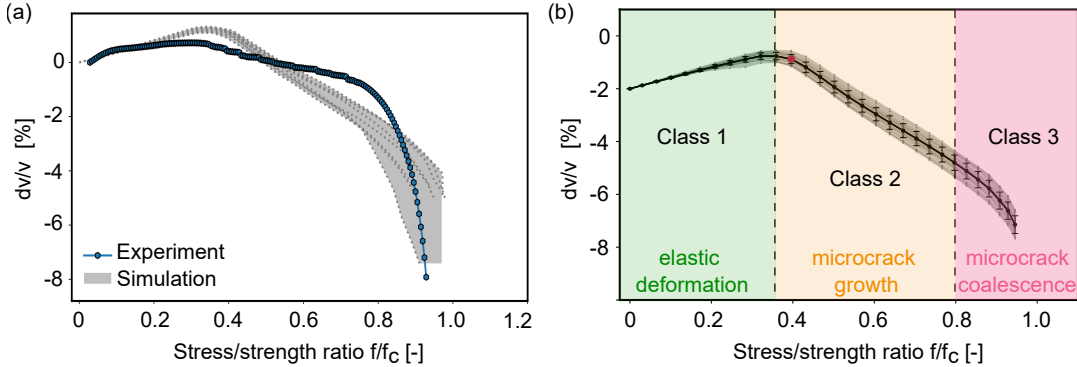


Figure 11: CWI analysis in concrete specimen under compression. (a) Validation of dv/v vs. applied stress at 0.3 ms time window; (b) Definition of damage classes based on CWI analysis of 300 wave simulations.

the simulation framework for subsequent damage classification tasks.

A total of 300 wave propagation simulations were conducted using the described setup, yielding 4500 ultrasonic signals for damage classification via CWI analysis (Niederleithinger et al., 2018). The stretching technique, combined with the auto-CWI method, was applied using a fixed 0–1 ms time window and a cross-correlation threshold of 0.7 to ensure consistent measurements. The computed relative velocity variations (dv/v) were plotted against normalized stress, revealing three distinct damage stages that define the classification labels as depicted in Figure 11(b). In the initial elastic regime (Class 1), dv/v increases linearly at a rate of 0.084% per MPa, peaking at 1.235%, which reflects elastic stiffening due to crack closure and pore compaction. In the subsequent phase (Class 2), spanning approximately 35–80% of the peak load, dv/v begins to decline gradually at -0.112% per MPa, indicating the development of diffuse microcracking that offsets any local stiffening effects. In the final phase (Class 3), beyond 80% of peak load, dv/v decreases sharply at -0.331% per MPa, marking the transition to localized damage and rapid stiffness degradation. At 42.1% of peak load, the cross-correlation coefficient drops below 0.7, triggering a reference signal update. Compared to experimental data, the simulated onset of damage in Class 2 occurs slightly earlier, potentially due to the absence of stable crack propagation in the Interfacial Transition Zones (ITZs). Across all sensor locations, moderate variability in dv/v response is observed, with the standard deviation increasing to 0.34% at higher load levels, capturing the inherent heterogeneity of damage evolution in concrete. Finally, the simulated dataset \mathcal{D}_s consists of 4500 samples in total, including 1740 samples of Class 1, 1680 samples of Class 2, and 1080 samples of Class 3.

5. Results and Discussion

5.1. Performance Comparison: Proposed Method vs. Plain 1D CNN

To better evaluate the performance improvement achieved by the proposed method in concrete damage classification, a plain 1D CNN was implemented as the baseline for comparison. The architecture and training configuration of the plain 1D CNN are kept identical to those of the proposed framework, except that both the DA and BYOL modules

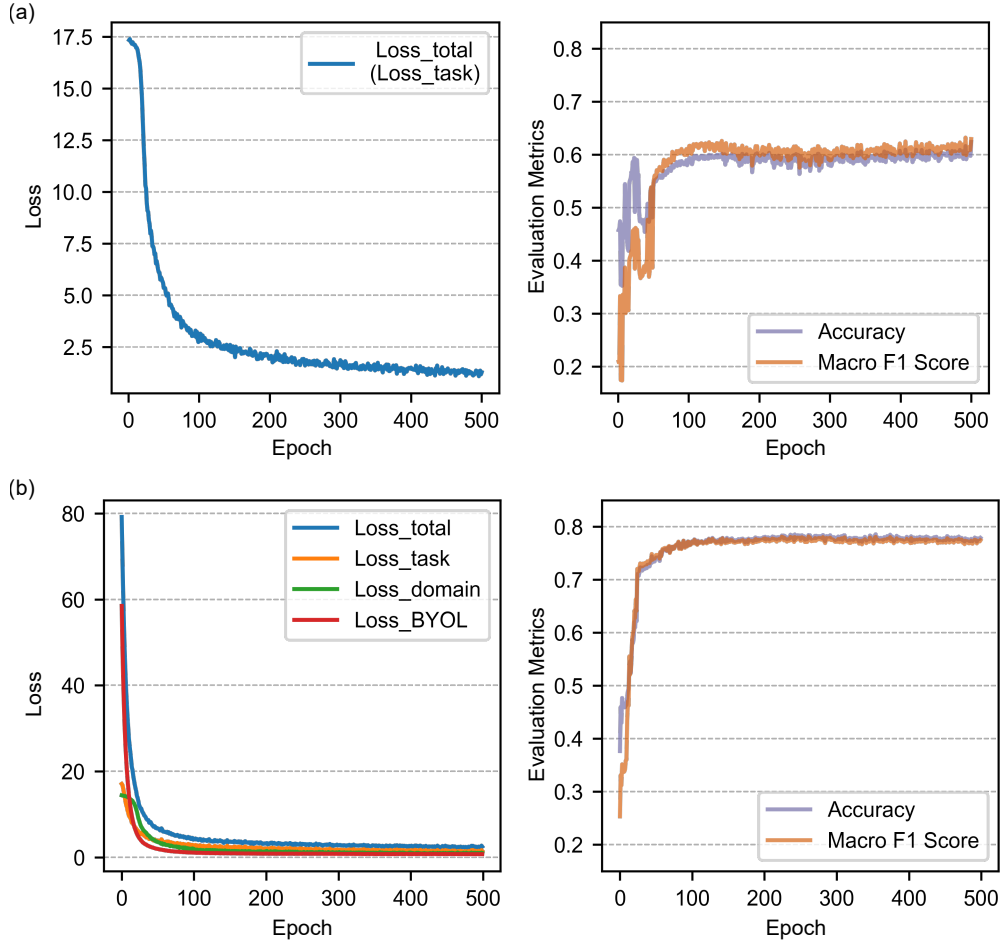


Figure 12: Training curves of (a) the plain 1D CNN and (b) the proposed method. Left: convergence of total loss and individual loss components over 500 epochs. Right: corresponding evolution of accuracy and macro F1 score on the experimental data.

were completely removed, resulting in a purely supervised model trained solely on simulated data.

Figure 12(a) and 12(b) illustrate the training dynamics of the plain 1D CNN and the proposed method, respectively, in terms of both loss convergence and classification performance on the experimental data. After 500 epochs, the total loss in both models converges, indicating successful optimization. For the proposed method, all components of the total loss stabilize over time, demonstrating that the joint training process of all modules remains stable and balanced throughout. Moreover, compared to the plain 1D CNN, the proposed method achieves not only higher accuracy and macro F1 scores on the experimental data, but also markedly reduced fluctuations throughout training, showing improved convergence behavior and greater training stability under domain shift.

Figures 13(a)-(d) compare the confusion matrices of the plain 1D CNN and the proposed method on both simulated and experimental datasets. On the simulated data (Figs. 13(a) and (b)), both models achieve high classification accuracy across all classes, indicating that

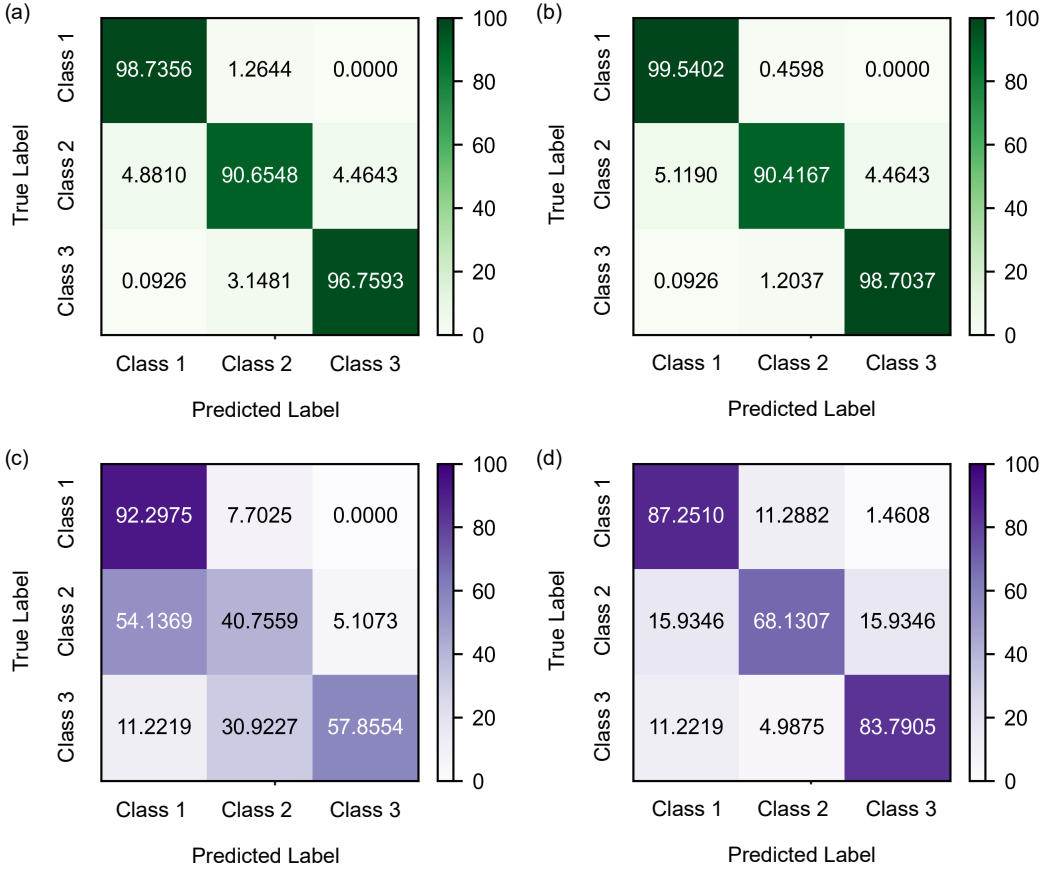


Figure 13: Confusion matrices of the plain 1D CNN and the proposed method on simulated and experimental datasets. (a) Plain 1D CNN on simulated data; (b) Proposed method on simulated data; (c) Plain 1D CNN on experimental data; (d) Proposed method on experimental data.

they can effectively learn from the source domain. However, a notable performance gap is observed when evaluated on the experimental data. The baseline model (Fig. 13(c)) shows excellent performance in identifying Class 1 (92.30%) but fails to generalize to Classes 2 and 3. In particular, 54.14% of Class 2 samples are misclassified as Class 1, and 30.92% of Class 3 samples are misclassified as Class 2, indicating poor cross-domain generalization and insufficient inter-class separability within the target domain. In contrast, the proposed method (Fig. 13(d)) significantly reduces misclassification across all classes. It achieves well-balanced predictions with class-wise accuracies of 87.38%, 68.13%, and 83.79% for Classes 1, 2, and 3, respectively.

Quantitatively, the plain 1D CNN achieves an overall accuracy of 0.6240 and a macro F1 score of 0.6294 on the experimental data. By comparison, the proposed method improves these metrics to 0.7803 and 0.7773, respectively, representing a substantial enhancement in classification performance. These results emphasize the effectiveness of the proposed domain adaptation framework in mitigating domain shift and achieving label-free concrete damage classification under real-world experimental conditions.

In terms of computational cost, the training time for the plain 1D CNN is approximately 1 minute and 10 seconds, while the proposed method requires 3 minutes and 9 seconds. Despite the additional neural network modules involved, this moderate increase in computational overhead is highly acceptable given the notable performance improvements. The proposed approach thus provides a practical and efficient solution for transferring knowledge from the simulation domain to the experiment domain, enabling reliable concrete damage identification based on coda waves.

5.2. Investigation on the Robustness of the Proposed Method

This section explores the robustness of the proposed method, both the plain 1D CNN and our method were independently trained and tested 50 times using different random seeds under identical experimental settings. Figure 14 presents the resulting accuracy distributions, which are visualized through histograms and kernel density estimate (KDE) plots.

As shown in Figure 14(a), the proposed method exhibits a highly concentrated accuracy distribution centered around 0.78, with low variance and a sharp unimodal KDE curve. In contrast, the plain 1D CNN shows a much broader distribution centered near 0.58, with a heavier left tail and more low-accuracy outliers. This contrast highlights the superior consistency and reliability in overall classification performance of the proposed method.

Figure 14(b) presents distinct distribution characteristics for Class 1 between the two models. While both models achieve relatively high accuracies, the proposed method demonstrates much tighter distribution, with its KDE sharply peaking around 0.88. In comparison, the baseline model shows a flatter and more dispersed distribution, suggesting greater sensitivity to variations in initialization or optimization dynamics across runs.

In Figure 14(c), which corresponds to Class 2, the performance gap becomes even more evident. The plain 1D CNN produces a wide and left-skewed distribution, with many runs falling below 0.4 in accuracy. On the other hand, the proposed method maintains a narrow distribution centered around 0.67, demonstrating a substantially improved ability to extract domain-invariant features for this particularly challenging Class.

Figure 14(d) presents the results for Class 3. The baseline model yields a distribution with moderate variance, reflecting fluctuations in performance across runs. In contrast, the proposed method exhibits a sharper peak near 0.84, with the majority of runs concentrated around this high-accuracy region. This indicates that the proposed method not only achieves better average performance but also delivers more stable and reliable predictions for Class 3.

In summary, the proposed method outperforms the plain 1D CNN in terms of both accuracy and robustness. Across all Classes, it not only improves average classification accuracy but also significantly reduces inter-run variability. Such robustness is particularly important in real-world SHM applications, where accurate and stable predictions are critical for structural integrity assessment and lifecycle management.

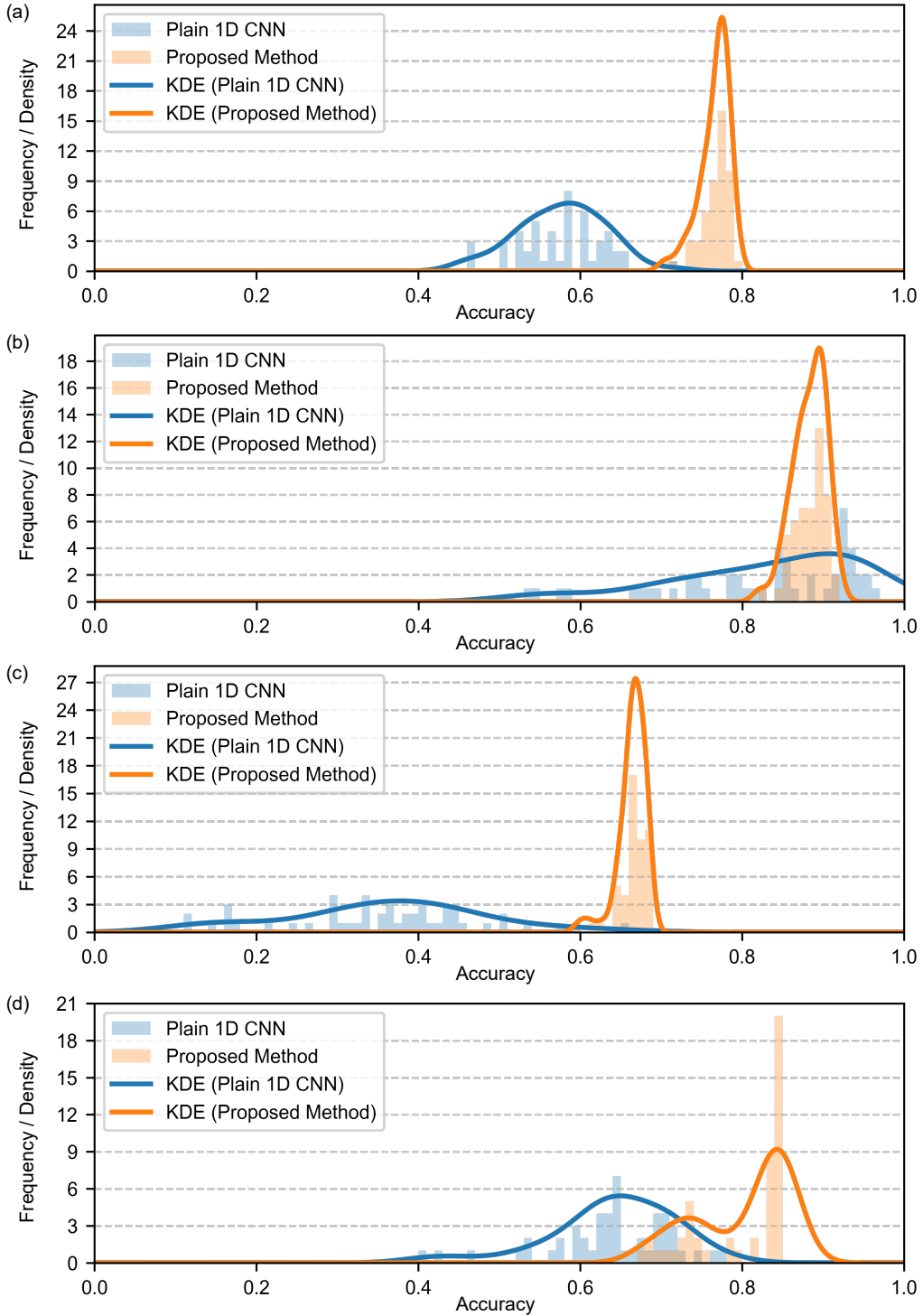


Figure 14: Comparison of classification robustness between the plain 1D CNN and the proposed method using histogram and kernel density estimation (KDE). Subfigures (a)–(d) illustrate the distribution of overall accuracy and class-wise accuracies for Classes 1, 2, and 3, respectively.

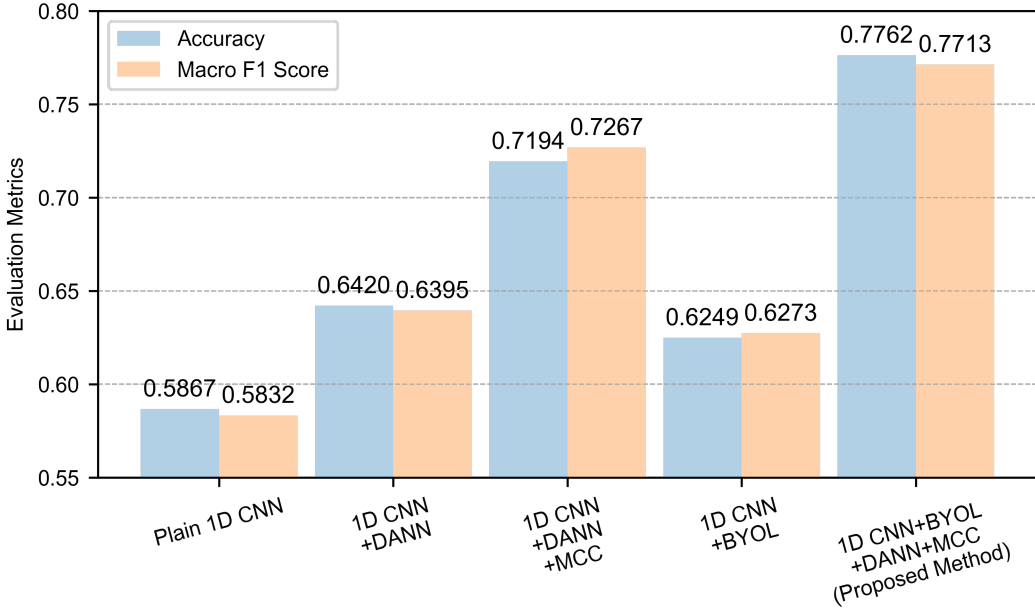


Figure 15: Results of the ablation study comparing the impact of different components in the proposed framework. The full model (rightmost group) combines Domain-Adversarial Neural Network (DANN), Minimum Class Confusion (MCC), and self-supervised learning (i.e., BYOL), and outperforms all other configurations in both accuracy and macro F1 score.

5.3. Ablation Study

In this section, an ablation study is carried out to evaluate the individual and joint contributions of its core components. Five model configurations are considered: (1) plain 1D CNN, (2) 1D CNN with DANN only, (3) 1D CNN with DANN and MCC, (4) 1D CNN with self-supervised learning via BYOL, and (5) the complete model combining DANN, MCC, and BYOL, referred to as the proposed method. We run each model for 10 times and report the average results. The performance comparison in terms of accuracy and macro F1 score is illustrated in Fig. 15.

The plain 1D CNN yields the lowest performance, with an accuracy of 0.5867 and a macro F1 score of 0.5832, reflecting its limited ability to generalize from simulated to experimental data. Introducing DANN without MCC leads to moderate improvement (accuracy: 0.6420, F1: 0.6395), indicating that domain adversarial training partially mitigates distribution shift but is still suboptimal when class confusion remains unaddressed.

When MCC is incorporated into the domain adaptation process, the performance improves significantly (accuracy: 0.7194, F1: 0.7267), confirming the benefit of reducing inter-class confusion in enhancing cross-domain classification. On the other hand, implementing BYOL alone also leads improvements over the baseline (accuracy: 0.6249, F1: 0.6273), suggesting that self-supervised learning facilitates the extraction of domain-transferable features from unlabeled experimental data.

Finally, the proposed method, which integrates DANN, MCC, and BYOL, achieves the

highest overall performance (accuracy: 0.7762, macro F1: 0.7713). This demonstrate that the three components work synergistically to improve the generalization under domain shift. All these results validate the soundness of the framework design and emphasize the importance of jointly addressing feature alignment, class confusion reduction, and self supervised learning for accurate and reliable concrete damage classification in real-world scenarios.

5.4. Comparison with Representative Domain Adaptation Methods

The superiority of the proposed method is evaluated through comparison with six representative DA techniques. All models adopt the same base architecture and are trained following the settings recommended in their original publications. For each model, results are averaged over ten independent runs to ensure statistical reliability. Specifically, the comparative models used are listed as follows:

- (1) JAN ([Long et al., 2017](#)): JAN (Joint Adaptation Network) alleviates domain shift by matching the joint distributions of multiple domain-specific layers across source and target domains using Joint Maximum Mean Discrepancy (JMMD).
- (2) MCD ([Saito et al., 2018](#)): MCD (Maximum Classifier Discrepancy) attempts to align source and target distributions by utilizing task-specific decision boundaries: two classifiers are trained to maximize their prediction discrepancy on target samples, while a feature generator learns to minimize this discrepancy in an adversarial manner.
- (3) MDD ([Zhang et al., 2019](#)): MDD (Margin Disparity Discrepancy) is a theoretically justified measurement that compares source and target distributions with asymmetric margin loss. It can be seamlessly integrated into an adversarial learning algorithm for domain adaptation.
- (4) DSAN ([Zhu et al., 2021](#)): DSAN (Deep Subdomain Adaptation Network) is a non-adversarial method that enhances DA by aligning subdomain distributions across source and target domains using Local Maximum Mean Discrepancy (LMMD).
- (5) MMSD ([Qian et al., 2023](#)): MMSD (Maximum Mean Square Discrepancy) is a novel discrepancy representation metric that extends traditional MMD by using both the mean and variance information of data distributions in reproducing kernel Hilbert space (RKHS).
- (6) DALN ([Chen et al., 2022](#)): DALN (Discriminator-free Adversarial Learning Network) reuses the task classifier as a discriminator to achieve explicit domain alignment and category distinguishment through a unified objective. It further introduces Nuclear-norm Wasserstein Discrepancy (NWD) to enhance prediction determinacy and diversity.

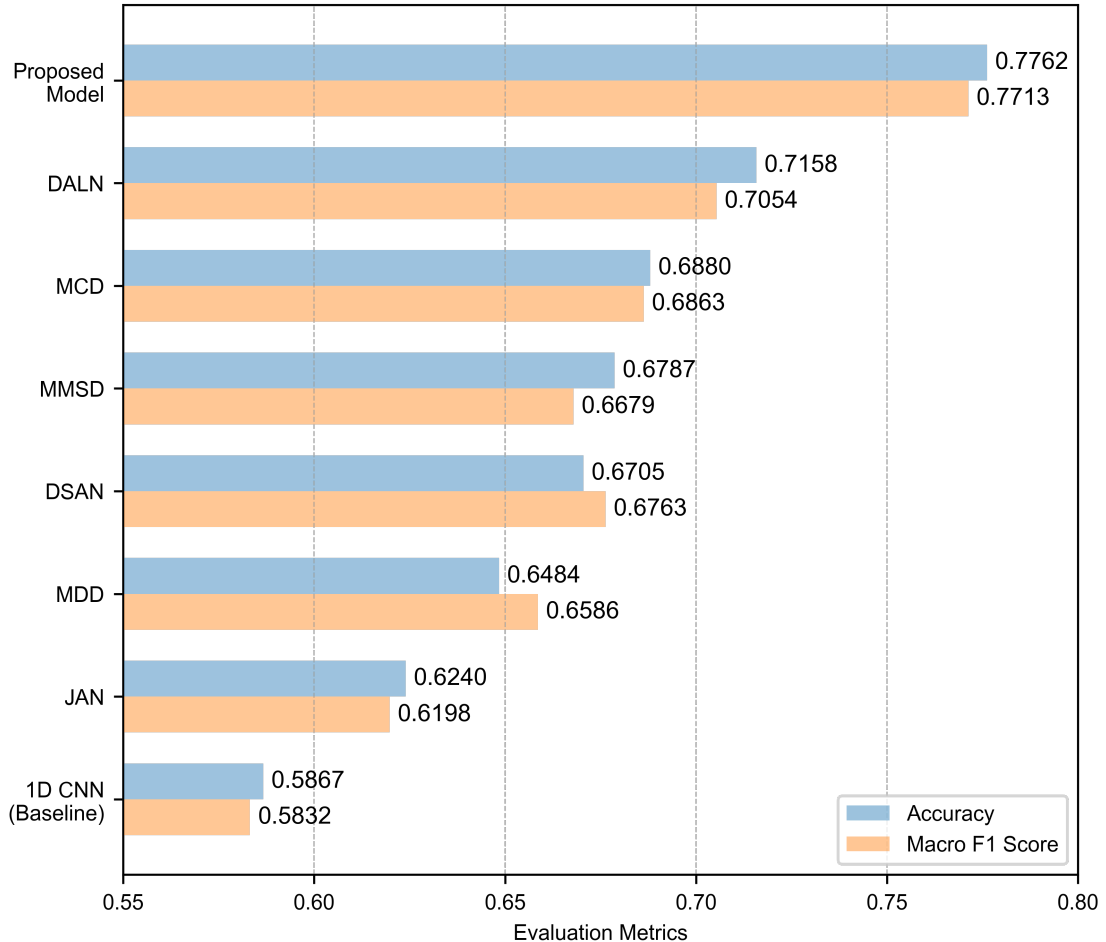


Figure 16: Performance comparison between the proposed method and six representative domain adaptation techniques on the experimental dataset.

Figure 16 presents the average results of these methods over ten runs in terms of accuracy and macro F1 score. All DA methods achieve noticeable improvements over the plain 1D CNN baseline. Among all the approaches evaluated, the proposed method has the best performance, with an accuracy of 0.7762 and a macro F1 score of 0.7713, which outperforms all other DA models. Notably, DALN also shows competitive results, with both metrics exceeding 0.7, and performs comparably to the 1D CNN+DANN+MCC configuration discussed in the previous ablation study section.

Figure 17 provides an overview of the confusion matrices corresponding to the six evaluated DA methods. In all cases, the diagonal elements dominate the matrices, indicating that each model achieves reasonable prediction accuracy across the three classes. Compared to the plain 1D CNN baseline (see Fig. 13(c)), all DA methods achieve moderate gains in classification performance. Among the six methods, DALN and MCD exhibit relatively higher and more balanced accuracy across all classes. In particular, both methods

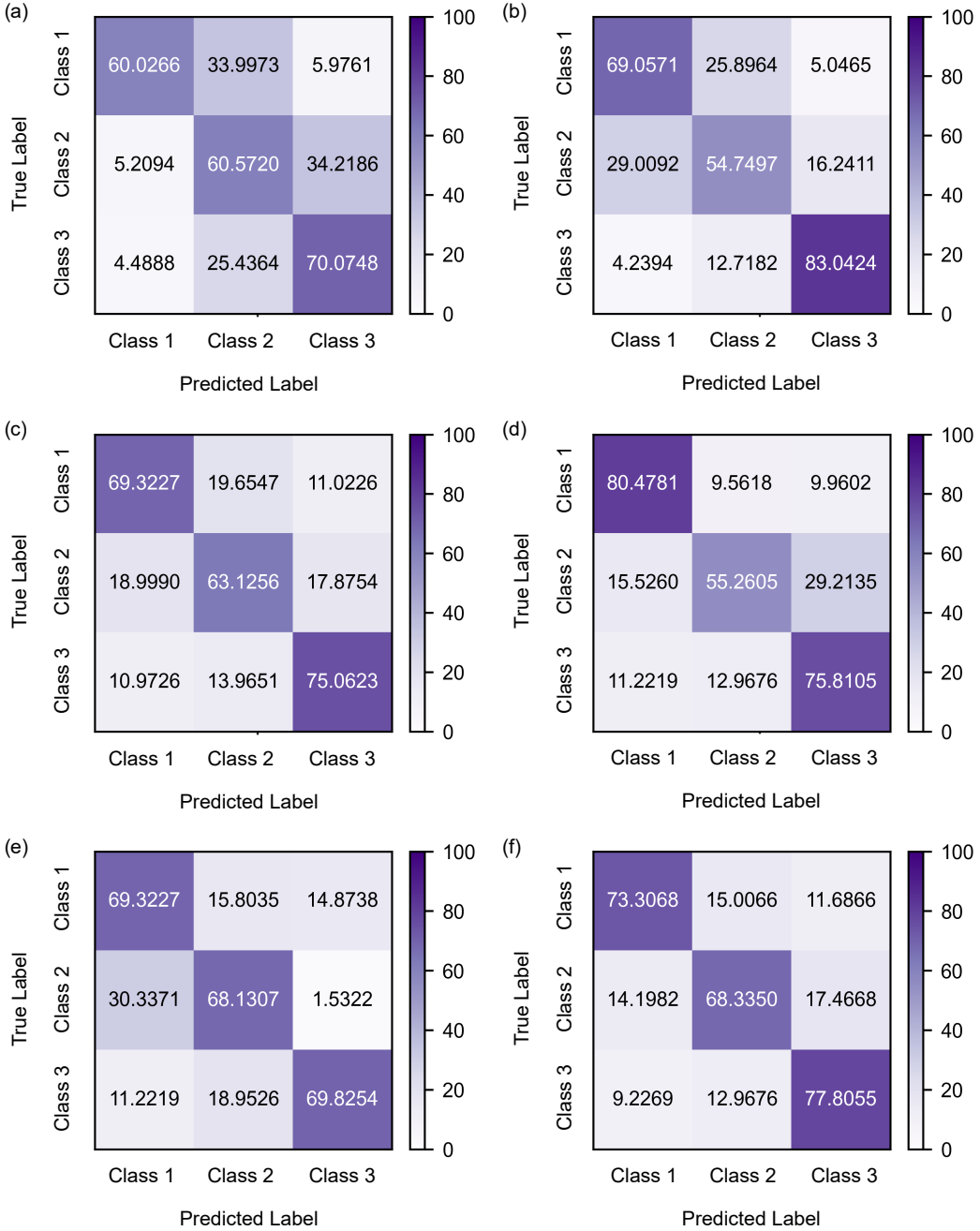


Figure 17: Confusion matrices of six representative domain adaptation methods on the experimental dataset: (a) JAN, (b) MDD, (c) DSAN, (d) MMSD, (e) MCD, and (f) DALN.

exceed 68% accuracy for Class 2, the most challenging due to its intermediate damage state, suggesting a stronger generalization to the target domain. Nevertheless, none of the methods surpass the proposed approach (see Fig. 13(d)), which achieves the highest overall accuracy and shows the most distinct separability between classes.

6. Conclusions

This work proposes a self-supervised domain adaptation framework for robust concrete damage classification. A virtual testing platform is firstly developed, which combines multiscale modeling of concrete damage with ultrasonic wave propagation simulations to generate abundant labeled synthetic data. The proposed approach bridges the domain gap between simulated and experimental data by integrating domain adversarial training, minimum class confusion, and the BYOL self-supervised learning paradigm, effectively transferring knowledge from the labeled simulated domain to the unlabeled experimental domain. Its key advantages are summarized as follows:

- (1) Accurate: The proposed method achieves an accuracy of 0.7762 and a macro F1 score of 0.7713, representing a significant improvement over the baseline plain 1D CNN (accuracy: 0.5867; macro F1 score: 0.5832).
- (2) Robust: Our method shows strong robustness across repeated trials. The resulting accuracy distributions are sharply peaked and narrow, as shown in the histogram and KDE plots, indicating consistent performance and stable convergence behavior under domain shift.
- (3) Fast: The framework has high computational efficiency. The training time increases by only about two minutes compared to the plain 1D CNN baseline. It is trained in an end-to-end manner without the need for separate offline pre-training or multi-stage optimization, making it well-suited for practical SHM applications.
- (4) Superior: Comparative evaluation against six representative domain adaptation methods (JAN, MDD, DSAN, MMSD, MCD, and DALN) highlights the superior generalization performance of the proposed framework under domain shift.

In future work, additional physical features or multimodal sensing data can be incorporated to further enrich the model input and enhance classification performance. Another important direction is to address class imbalance in real-world data, which may affect the model's generalization under practical scenarios. Moreover, since the current dataset mainly focuses on compressive damage in concrete, extending the framework to include tensile damage scenarios will be an important step toward broader applicability in structural health monitoring.

While this study is conducted under controlled laboratory conditions, real-world structures often involve more complex boundary conditions and long-term degradation mechanisms. Therefore, adapting the proposed framework for in-situ monitoring applications can also be an important future direction. In this context, knowledge gained from specimen-level damage characterization is expected to serve as a foundation for developing advanced strategies for structural-level damage identification, thereby enabling more effective and reliable assessment of concrete structures in practice.

7. Acknowledgment

The first author acknowledges the support from the China Scholarship Council (CSC) under grant 202006260038, the Bridging Scholarship from the Research Department Sub-surface Modeling & Engineering (RDSME) of Ruhr University Bochum, and the Scholarship of Wilhelm and Günter Esser Foundation from the Research School of Ruhr University Bochum. The authors gratefully acknowledge the exchange and numerous discussion with the Chair of Materials Science and Testing at Technical University Munich, in particular with Prof. Christoph Gehlen, which were helpful for the interpretation of experimental data. The authors would also like to thank the German Research Foundation (DFG) for their financial support in the framework of Subprojects RUB1, TUM1 of the Research Unit FOR 2825 (project number 398216472).

References

- Brough, D. B., Wheeler, D., and Kalidindi, S. R. (2017). Materials knowledge systems in python—a data science framework for accelerated development of hierarchical materials. *Integrating materials and manufacturing innovation*, 6(1):36–53.
- Cecen, A., Fast, T., and Kalidindi, S. R. (2016). Versatile algorithms for the computation of 2-point spatial correlations in quantifying material structure. *Integrating Materials and Manufacturing Innovation*, 5(1):1–15.
- Chen, L., Chen, H., Wei, Z., Jin, X., Tan, X., Jin, Y., and Chen, E. (2022). Reusing the task-specific classifier as a discriminator: Discriminator-free adversarial domain adaptation. In *Proceedings of the IEEE/CVF Conference on Computer Vision and Pattern Recognition (CVPR)*, pages 7181–7190.
- Chen, T., Kornblith, S., Norouzi, M., and Hinton, G. (2020). A simple framework for contrastive learning of visual representations. In III, H. D. and Singh, A., editors, *Proceedings of the 37th International Conference on Machine Learning*, volume 119, pages 1597–1607. PMLR.
- Diewald, F., Epple, N., Kraenkel, T., Gehlen, C., and Niederleithinger, E. (2022). Impact of external mechanical loads on coda waves in concrete. *Materials*, 15.
- Ganin, Y., Ustinova, E., Ajakan, H., Germain, P., Larochelle, H., Laviolette, F., March, M., and Lempitsky, V. (2016). Domain-adversarial training of neural networks. *Journal of Machine Learning Research*, 17:1–35.
- Giglioni, V., Poole, J., Venanzi, I., Ubertini, F., and Worden, K. (2024). A domain adaptation approach to damage classification with an application to bridge monitoring. *Mechanical Systems and Signal Processing*, 209:111135.
- Grabke, S., Bletzinger, K. U., and Wüchner, R. (2022). Development of a finite element-based damage localization technique for concrete by applying coda wave interferometry. *Engineering Structures*, 269:114585.
- Grabke, S., Clauß, F., Bletzinger, K.-U., Ahrens, M. A., Mark, P., and Wüchner, R. (2021). Damage detection at a reinforced concrete specimen with coda wave interferometry. *Materials*, 14.
- Grill, J.-B., Strub, F., Altché, F., Tallec, C., Richemond, P., Buchatskaya, E., Doersch, C., Pires, B. A., Guo, Z., Azar, M. G., Piot, B., koray kavukcuoglu, Munos, R., and Valko, M. (2020). Bootstrap your own latent - a new approach to self-supervised learning. In Larochelle, H., Ranzato, M., Hadsell, R., Balcan, M. F., and Lin, H., editors, *Advances in Neural Information Processing Systems*, volume 33, pages 21271–21284. Curran Associates, Inc.

- Gu, Y., Ai, Q., Xu, Z., Yao, L., Wang, H., Huang, X., and Yuan, Y. (2024). Cost-effective image recognition of water leakage in metro tunnels using self-supervised learning. *Automation in Construction*, 167:105678.
- Gui, J., Chen, T., Zhang, J., Cao, Q., Sun, Z., Luo, H., and Tao, D. (2024). A survey on self-supervised learning: Algorithms, applications, and future trends. *IEEE Transactions on Pattern Analysis and Machine Intelligence*, 46:9052–9071.
- He, K., Fan, H., Wu, Y., Xie, S., and Girshick, R. (2020). Momentum contrast for unsupervised visual representation learning. In *Proceedings of the IEEE/CVF Conference on Computer Vision and Pattern Recognition (CVPR)*.
- Hoxha, E., Feng, J., Sengupta, A., Kirakosian, D., He, Y., Shang, B., Gjinofci, A., and Xiao, J. (2025). Contrastive learning for robust defect mapping in concrete slabs using impact echo. *Construction and Building Materials*, 461:139829.
- Huang, K., Ren, Z., Zhu, L., Lin, T., Zhu, Y., Zeng, L., and Wan, J. (2025). Intra-domain self generalization network for intelligent fault diagnosis of bearings under unseen working conditions. *Advanced Engineering Informatics*, 64:102997.
- Jiang, F., Kuang, Y., Li, T., Zhang, S., Wu, Z., Feng, K., and Li, W. (2025). Towards enhanced interpretability: A mechanism-driven domain adaptation model for bearing fault diagnosis across operating conditions. *Mechanical Systems and Signal Processing*, 225:112244.
- Jiang, F., Lin, W., Wu, Z., Zhang, S., Chen, Z., and Li, W. (2024). Fault diagnosis of gearbox driven by vibration response mechanism and enhanced unsupervised domain adaptation. *Advanced Engineering Informatics*, 61:102460.
- Jin, Y., Wang, X., Long, M., and Wang, J. (2020). Minimum class confusion for versatile domain adaptation. In Horst, Thomas, B., Andrea, F. J.-M. V., and Bischof, editors, *Computer Vision – ECCV 2020*, pages 464–480. Springer International Publishing.
- Karniadakis, G. E., Kevrekidis, I. G., Lu, L., Perdikaris, P., Wang, S., and Yang, L. (2021). Physics-informed machine learning. *Nature Reviews Physics*, 3:422–440.
- Kiranyaz, S., Avci, O., Abdeljaber, O., Ince, T., Gabbouj, M., and Inman, D. J. (2021). 1d convolutional neural networks and applications: A survey. *Mechanical Systems and Signal Processing*, 151:107398.
- Li, Z., He, W., Ren, W., Li, Y., Li, Y., and Cheng, H. (2023). Damage detection of bridges subjected to moving load based on domain-adversarial neural network considering measurement and model error. *Engineering Structures*, 293:116601.
- Li, Z., Liu, F., Yang, W., Peng, S., and Zhou, J. (2022). A survey of convolutional neural networks: Analysis, applications, and prospects. *IEEE Transactions on Neural Networks and Learning Systems*, 33:6999–7019.

- Li, Z., Weng, S., Xia, Y., Yu, H., Yan, Y., and Yin, P. (2024). Cross-domain damage identification based on conditional adversarial domain adaptation. *Engineering Structures*, 321:118928.
- Liu, L., Li, S., Zheng, M., Wang, Y., Shen, J., Shi, Z., Xia, C., and Zhou, J. (2024). Identification of rock discontinuities by coda wave analysis while borehole drilling in deep buried tunnels. *Tunnelling and Underground Space Technology*, 153:105969.
- Liu, X., Yoo, C., Xing, F., Oh, H., Fakhri, G. E., Kang, J.-W., and Woo, J. (2022). Deep unsupervised domain adaptation: A review of recent advances and perspectives. *APSIPA Transactions on Signal and Information Processing*, 11.
- Liu, X., Zhang, F., Hou, Z., Mian, L., Wang, Z., Zhang, J., and Tang, J. (2023). Self-supervised learning: Generative or contrastive. *IEEE Transactions on Knowledge and Data Engineering*, 35:857–876.
- Liu, Y. and Fang, S. E. (2024). Cross-domain structural damage identification using transfer learning strategy. *Engineering Structures*, 311:118171.
- Liu, Z., Bessa, M. A., and Liu, W. K. (2016). Self-consistent clustering analysis: An efficient multi-scale scheme for inelastic heterogeneous materials. *Computer Methods in Applied Mechanics and Engineering*, 306:319–341.
- Long, M., Zhu, H., Wang, J., and Jordan, M. I. (2017). Deep transfer learning with joint adaptation networks. In Precup, D. and Teh, Y. W., editors, *Proceedings of the 34th International Conference on Machine Learning*, volume 70, pages 2208–2217. PMLR.
- Lu, L., Jin, P., Pang, G., Zhang, Z., and Karniadakis, G. E. (2021). Learning nonlinear operators via deeponet based on the universal approximation theorem of operators. *Nature Machine Intelligence*, 3:218–229.
- Matouš, K., Geers, M. G., Kouznetsova, V. G., and Gillman, A. (2017). A review of predictive nonlinear theories for multiscale modeling of heterogeneous materials. *Journal of Computational Physics*, 330:192–220.
- Niederleithinger, E., Wang, X., Herbrand, M., and Müller, M. (2018). Processing ultrasonic data by coda wave interferometry to monitor load tests of concrete beams. *Sensors*, 18(6):1971.
- Pan, S. J. and Yang, Q. (2010). A survey on transfer learning. *IEEE Transactions on Knowledge and Data Engineering*, 22:1345–1359.
- Pang, B., Liu, Q., Xu, Z., Sun, Z., Hao, Z., and Song, Z. (2024). Fault vibration model driven fault-aware domain generalization framework for bearing fault diagnosis. *Advanced Engineering Informatics*, 62:102620.

- Planès, T. and Larose, E. (2013). A review of ultrasonic coda wave interferometry in concrete. *Cement and Concrete Research*, 53:248–255.
- Qian, Q., Wang, Y., Zhang, T., and Qin, Y. (2023). Maximum mean square discrepancy: A new discrepancy representation metric for mechanical fault transfer diagnosis. *Knowledge-Based Systems*, 276:110748.
- Qu, S., Hilloulin, B., Saliba, J., Sbartaï, M., Abraham, O., and Tournat, V. (2023). Imaging concrete cracks using nonlinear coda wave interferometry (incwi). *Construction and Building Materials*, 391:131772.
- Raissi, M., Perdikaris, P., and Karniadakis, G. E. (2019). Physics-informed neural networks: A deep learning framework for solving forward and inverse problems involving nonlinear partial differential equations. *Journal of Computational Physics*, 378:686–707.
- Saenger, E. H., Shapiro, S. A., and Keehm, Y. (2005). Seismic effects of viscous biot-coupling: Finite difference simulations on micro-scale. *Geophysical Research Letters*, 32:L14310.
- Saito, K., Watanabe, K., Ushiku, Y., and Harada, T. (2018). Maximum classifier discrepancy for unsupervised domain adaptation. In *Proceedings of the IEEE Conference on Computer Vision and Pattern Recognition (CVPR)*, pages 3723–3732.
- Schepp, L. L., Ahrens, B., Balcewicz, M., Duda, M., Nehler, M., Osorno, M., Uribe, D., Steeb, H., Nigon, B., Stöckhert, F., Swanson, D. A., Siegert, M., Gurris, M., and Saenger, E. H. (2020). Digital rock physics and laboratory considerations on a high-porosity volcanic rock. *Scientific Reports*, 10.
- Shan, S., Liu, Z., Cheng, L., and Pan, Y. (2022). Metamaterial-enhanced coda wave interferometry with customized artificial frequency-space boundaries for the detection of weak structural damage. *Mechanical Systems and Signal Processing*, 174:109131.
- Snieder, R. (2006). The theory of coda wave interferometry. *Pure and Applied Geophysics*, 163:455–473.
- Snieder, R., Grêt, A., Douma, H., and Scales, J. (2002). Coda wave interferometry for estimating nonlinear behavior in seismic velocity. *Science*, 295:2253–2255.
- Sträter, N., Clauß, F., Ahrens, M. A., and Mark, P. (2025). Detection of tendon breaks in prestressed concrete structures using coda wave interferometry. *Structural Concrete*, 26:3319–3332.
- Talaei, S., Zhu, X., Li, J., Yu, Y., and Chan, T. H. (2025). A hybrid domain adaptation approach for estimation of prestressed forces in prestressed concrete bridges under moving vehicles. *Engineering Structures*, 330:119904.

- Vu, G., Diewald, F., Timothy, J. J., Gehlen, C., and Meschke, G. (2021a). Reduced order multiscale simulation of diffuse damage in concrete. *Materials*, 14:3830.
- Vu, G., Timothy, J. J., Saenger, E. H., Gehlen, C., and Meschke, G. (2025). A virtual lab for damage identification in concrete using coda wave interferometry. *Structure and Infrastructure Engineering*, pages 1–16.
- Vu, G., Timothy, J. J., Singh, D. S., Saydak, L. A., Saenger, E. H., and Meschke, G. (2021b). Numerical simulation-based damage identification in concrete. *Modelling*, 2:355–369.
- Wang, S., Hu, M., Tang, L., Kim, M., and Aw, K. C. (2025). Displacement reconstruction with frequency domain-invariant representation for enhancing track damage identification. *Engineering Structures*, 328:119693.
- Wang, X., Chakraborty, J., and Niederleithinger, E. (2021). Noise reduction for improvement of ultrasonic monitoring using coda wave interferometry on a real bridge. *Journal of Nondestructive Evaluation*, 40.
- Wang, X. and Xia, Y. (2022). Knowledge transfer for structural damage detection through re-weighted adversarial domain adaptation. *Mechanical Systems and Signal Processing*, 172:108991.
- Weng, X., Huang, Y., Li, Y., Yang, H., and Yu, S. (2023). Unsupervised domain adaptation for crack detection. *Automation in Construction*, 153:104939.
- Xiao, Y., Shao, H., Yan, S., Wang, J., Peng, Y., and Liu, B. (2025). Domain generalization for rotating machinery fault diagnosis: A survey. *Advanced Engineering Informatics*, 64:103063.
- Xiong, Q., Xia, Y., Xiong, H., Yuan, C., Chen, J., and Kong, Q. (2025). Re-acgan: Structural damage identification with class-imbalance reweighted acgan for data augmentation. *Engineering Structures*, 329:119814. 1d cnn as baseline.
- Xu, C., Cao, B. T., Yuan, Y., and Meschke, G. (2023). Transfer learning based physics-informed neural networks for solving inverse problems in engineering structures under different loading scenarios. *Computer Methods in Applied Mechanics and Engineering*, 405:1–41.
- Xu, C., Cao, B. T., Yuan, Y., and Meschke, G. (2024). A multi-fidelity deep operator network (deponet) for fusing simulation and monitoring data: Application to real-time settlement prediction during tunnel construction. *Engineering Applications of Artificial Intelligence*, 133:108156.
- Yi, S., Yang, C., Sun, X., Li, J., Wang, L., Gao, C., and Yu, Y. (2024). Evaluation of compressive damage in concrete using ultrasonic nonlinear coda wave interferometry. *Ultrasonics*, 144:107438.

- Zhang, X., Zhu, X., Wang, Y., and Li, J. (2025). Structural damage detection based on transmissibility functions with unsupervised domain adaptation. *Engineering Structures*, 322:119142.
- Zhang, Y., Liu, T., Long, M., and Jordan, M. (2019). Bridging theory and algorithm for domain adaptation. In Chaudhuri, K. and Salakhutdinov, R., editors, *Proceedings of the 36th International Conference on Machine Learning*, volume 97, pages 7404–7413. PMLR.
- Zhu, P., Deng, L., Tang, B., Yang, Q., and Li, Q. (2025). Digital twin-enabled entropy regularized wavelet attention domain adaptation network for gearboxes fault diagnosis without fault data. *Advanced Engineering Informatics*, 64:103055.
- Zhu, Y., Zhuang, F., Wang, J., Ke, G., Chen, J., Bian, J., Xiong, H., and He, Q. (2021). Deep subdomain adaptation network for image classification. *IEEE Transactions on Neural Networks and Learning Systems*, 32:1713–1722.